# Multi-fidelity surrogate optimization of an electrothermal ice protection system for in-flight anti-icing

Maziyar Ghasemnezhad [a], Esmaeil Esmaeilifar [a], Rho Shin Myong [a, *]

[a] School of Mechanical and Aerospace Engineering, and ACTRC, Gyeongsang National University, 501 Jinjudaero, Jinju, Gyeongnam 52828, South Korea

*Corresponding author. E-mail address: *myong@gnu.ac.kr* (R.S. Myong)

## Abstract

This study proposes a novel multi-fidelity surrogate optimization (MFSO) framework for evaluating and optimizing an electrothermal ice protection system for in-flight anti-icing. This approach effectively integrates high-fidelity and low-fidelity simulations to significantly reduce the number of training samples required to train an accurate surrogate model, thereby lowering computational costs without compromising accuracy. The surrogate model was constructed via proper orthogonal decomposition (POD) and multi-fidelity Gaussian process regression (MFGPR). To perform high-fidelity simulations of the electrothermal anti-icing process, a unified finite volume framework was employed. This framework efficiently combines several in-house solvers, including a compressible Navier–Stokes–Fourier (NSF) airflow solver, an Eulerian droplet impingement solver, a partial differential equation (PDE)-based ice accretion solver, and a multilayer heat conduction solver. The optimization framework minimizes total electric power consumption while satisfying regime-specific constraints in both running-wet and evaporative modes. The search for optimal heater power distributions is guided by the mesh adaptive direct search (MADS) algorithm. Our findings show that the multi-fidelity surrogate model reduces training cost by 75% by lowering the number of required high-fidelity simulations from 400 in the single-fidelity approach to 100. The optimization results achieved up to 38.5% reduction in total electric power consumption for the running-wet regime and 40% for the evaporative regime under representative operational constraints for the NACA0012 airfoil.

**Keywords:** Multi-fidelity surrogate optimization; Aircraft icing; Electrothermal anti-icing; Gaussian process regression; Mesh adaptive direct search

## 1. Introduction

Aircraft icing presents a substantial and ongoing risk to both aviation safety and operational effectiveness [1-3]. Icing occurs when supercooled water droplets collide with aircraft surfaces, most notably the leading edges, resulting in the accumulation of ice [4, 5]. In-flight icing conditions refer to the atmospheric and flight environments encountered during aircraft operation within clouds and are typically characterized by free-stream velocity, ambient temperature, liquid water content (LWC), and median volume diameter (MVD), as defined from in-flight icing envelopes [5, 6]. The accretion of ice significantly compromises aircraft control by affecting critical aerodynamic surfaces, such as ailerons, flaps, slats, rudder, and elevators. Beyond control surfaces, ice accumulation can also diminish visibility through the windshield and disrupt instrument measurements, leading to imprecise readings from pitot and static tubes [7, 8]. Moreover, the ingestion of ice crystals can severely degrade engine performance. Given these critical hazards, ice protection systems (IPS) are essential for maintaining flight safety and operational integrity across all types of air vehicles, including urban air mobility (UAM) systems, airplanes, helicopters, and gliders [9, 10]. IPS are crucial for mitigating the performance degradation and engine inefficiency that arise from ice accretion [11-13].

IPS are broadly categorized into mechanical, thermal, and chemical systems, each of which has distinct operational characteristics and implications for aircraft performance. Mechanical systems, such as pneumatic boots, perform de-icing by shedding accumulated ice. However, their application is generally limited to specific components, and they are often unsuitable for comprehensive protection across diverse aircraft components or unmanned aerial vehicles. Chemical systems (weeping wing) prevent ice by spreading de-icing fluid over critical surfaces. They offer simplicity but add weight, require fluid storage, and have limited endurance. Thermal systems include traditional hot air (bleed air) methods as well as electrothermal ice protection systems (ETIPS), which employ electrical power to heat embedded elements. Because ETIPS are not reliant on bleed air, they improve engine efficiency, reduce weight, and mitigate environmental impact.

IPS operates in two fundamental modes—de-icing and anti-icing—each tailored to specific operational needs. De-icing methods allow ice to form on aircraft surfaces before the system is activated to remove it, and can be applied both during flight and on the ground [7, 14]. Conversely, anti-icing systems aim to prevent ice accretion altogether by inhibiting the adherence of supercooled water droplets [15, 16].

Thermal anti-icing strategies can be further categorized into evaporative mode and running wet mode. The evaporative mode maintains an ice-free surface by fully evaporating water within the protected zone, effectively preventing the formation of runback ice. Although this approach significantly enhances safety, it requires high-power density, which in turn increases energy consumption. In comparison, the running wet mode offers a more energy-efficient solution by enabling the use of smaller generators. However, the wet mode requires careful IPS design and precise heater power distribution to ensure that residual water does not refreeze downstream, which could lead to dangerous ice accumulation in unprotected regions [3, 5].

ETIPS offer the advantage of customized heat distribution to enhance energy efficiency, yet they inherently consume a substantial amount of energy, especially during continuous anti-icing operations [5]. Accordingly, a precise and careful strategy for optimizing heater power density across all operational regimes and modes must be established to ensure the best possible power efficiency. However, optimizing heat distribution requires multiple direct simulations, and minimizing ETIPS power density involves costly high-fidelity computations. Consequently, the use of surrogate models is essential to speed up the optimization process.

The computational modeling of electrothermal IPS involves a detailed multiphysics framework that integrates various solvers to represent different physical processes. An air solver is used to simulate the airflow around the aircraft and determine the heat transfer coefficient and wall shear stress. The droplet solver handles the air-droplet mixture to estimate droplet distribution and impingement behavior on the surface. The ice solver is employed to model the runback water film and surface ice accretion or melting based on mass and energy balance equations. Additionally, a heat conduction solver computes the temperature profile both within and on the surface of the multilayer composite structure. The thermal coupling between these solvers is captured through the conjugate heat transfer method.

In icing research, high-fidelity simulations of aircraft icing involve solving the Navier–Stokes–Fourier (NSF) equation for airflow, and a partial differential equation (PDE)-based thermodynamic model for ice solver, while low-fidelity simulations utilize panel methods or potential flow solvers for airflow and the Messinger model as the ice accretion solver. However, in this study, we define fidelity based on the thermal modeling of the composite and its interaction with the air/water film. In other words, for the ETIPS high-fidelity simulation, a CHT simulation is performed, which includes solving heat conduction in the solid. The mid-fidelity model considers heater power using a uniform equivalent thermal layer with specified heat flux, and the low-fidelity model neglects substrate conduction entirely.

Table 1 presents a comparison of various approaches that have been developed for optimizing ETIPS. Earlier studies on surrogate-based optimization have primarily relied on high-fidelity simulations, which are computationally expensive, or on mid-fidelity and low-fidelity simulations, which are computationally inexpensive but suffer reduced accuracy. For instance, Pourbagian et al. [17] developed a surrogate-based optimization framework for the anti-icing mode of ETIPS for high-fidelity simulations. To achieve this, they employed a Kriging surrogate model to efficiently approximate the complex simulations. Additionally, the mesh adaptive direct search (MADS) algorithm was utilized to perform the optimization process, ensuring convergence toward optimal heater configurations while minimizing the objectives [18]. In subsequent works [19, 20], they incorporated a range of design variables, objective functions, and constraints to address the problem's inherent difficulty. Building on this foundation, Targui and Habashi [21] extended the surrogate-based optimization approach to three-dimensional geometries. Meanwhile, Jung et al. [22] introduced a surrogate model for evaluating ETIPS performance in a rotorcraft engine air intake, although their work did not involve any optimization.

**Table 1**
Comparison of existing surrogate-based ETIPS optimization studies and the proposed multi-fidelity approach.

| Study | Fidelity level | Computational cost | Surrogate model | Optimization | Key features |
|---|---|---|---|---|---|
| **Pourbagian et al. [14-17]** | High-fidelity | High | Single fidelity Surrogate model | MADS-algorithm | Surrogate-based optimization for anti-icing, heater power optimization |
| **Targui & Habashi [18]** | High-fidelity | High | Single fidelity Surrogate model | MADS-algorithm | Extended surrogate-based optimization to 3D geometries |
| **Jung et al. [19]** | High-fidelity | High | Single fidelity Surrogate model | No optimization | Surrogate model for ETIPS performance evaluation |
| **Gutiérrez et al. [20]** | Mid-fidelity | Mid | Single fidelity Surrogate model | Genetic algorithm | Heater power optimization |
| **Gulia et al. [21]** | Mid-fidelity | Mid | Single fidelity Surrogate model | MADS algorithm | Robust design optimization under uncertainty |
| **Present Study** | High-fidelity | Low | Multi-fidelity surrogate model | MADS-algorithm | Reduces HF sample requirements, maintains HF-level accuracy, and optimizes heater power |

On the other hand, Galia and Gutiérre [23, 24] used mid-fidelity simulations for ETIPS design by modeling heater power through a uniform equivalent thermal property layer within the substrate (via electrical analogy) and applying specified heat flux boundary conditions to create training data for surrogate modeling. In these studies, they initially optimized the heater power density to ensure ice-free surfaces using genetic algorithms, then incorporated robust design optimization techniques under uncertainty conditions using the MADS algorithm.

The primary objective in ETIPS surrogate modeling is to replace computationally intensive solvers with efficient and accurate surrogates capable of capturing both conjugate heat transfer and the structural complexity of composites with embedded heaters. As mentioned earlier, high-fidelity simulations of ETIPS are computationally expensive, while low-fidelity simulations are less accurate. Addressing this trade-off requires strategies that minimize reliance on high-fidelity data while maintaining sufficient predictive accuracy for training our surrogate model.

This approach aligns with multi-fidelity optimization, which integrates models of varying fidelity to achieve accurate solutions while reducing the computational cost of high-fidelity evaluations [25]. By leveraging low-fidelity data to guide high-fidelity surrogate modeling, multi-fidelity methods significantly reduce computational demands [26-33].

*To overcome the limitations of existing methods, this study proposes a novel multi-fidelity surrogate model (MFSM) designed to substantially reduce the number of required high-fidelity training samples while maintaining predictive performance.* By effectively integrating low-fidelity data, the proposed method achieves high-fidelity-level accuracy with significantly lower computational cost, offering a practical solution to the efficiency–accuracy trade-off in ETIPS modeling.

This paper is organized as follows: Section 2 introduces the numerical framework for the ETIPS analysis, including both high-fidelity and low-fidelity simulation models and their respective solvers. Section 3 presents the proposed multi-fidelity surrogate-based optimization methodology, providing a detailed problem formulation, surrogate model structure, and optimization algorithm. In Section 4, the results of the multi-fidelity optimization are demonstrated for two anti-icing modes, evaporative and running-wet regimes, under various constraint formulations. Lastly, Section 5 offers conclusions, outlines potential directions for future work, and discusses the advantages and key achievements of the proposed multi-fidelity optimization strategy.

## 2. Numerical approach to ETIPS analysis

This section presents the numerical models employed for electrothermal ice protection system (ETIPS) simulations, encompassing both high-fidelity and low-fidelity approaches and their corresponding solvers. In general, high-fidelity simulations require solving the complete set of governing partial differential equations (PDEs), such as the Navier–Stokes–Fourier equations, whereas low-fidelity approaches utilize simplified empirical correlations that significantly reduce computational cost. Although all solvers implemented in this study inherently solve PDEs and could technically be classified as high-fidelity, the distinction here is based on the level of thermal modeling detail. The high-fidelity model incorporates a full conduction solver within the solid substrate, while the low-fidelity model neglects internal heat conduction and applies heat flux solely at the boundary.

As illustrated in Fig. 1a, the high-fidelity framework integrates air, droplet, ice, and conduction solvers to accurately capture heat transfer and ice accretion processes. The airflow and droplet impingement simulations are performed once under clean-air conditions at the beginning of the procedure and remain unchanged throughout the anti-icing simulation. The density, velocity, and pressure fields computed by the air solver are supplied to the droplet solver, while the wall shear stress and convective heat-transfer coefficient from the air solver, together with the droplet collection efficiency from the droplet solver, are transferred to the ice solver. Heat conduction within the solid is computed using the conduction solver, which is tightly coupled with the ice solver through sub-iterations to ensure consistent wall temperature predictions. In contrast, as shown in Fig. 1b, the low-fidelity solver preserves the sequential air, droplet, and ice solver structure but omits the conduction solver and the associated tight coupling, thereby eliminating sub-iterations and significantly reducing computational complexity.

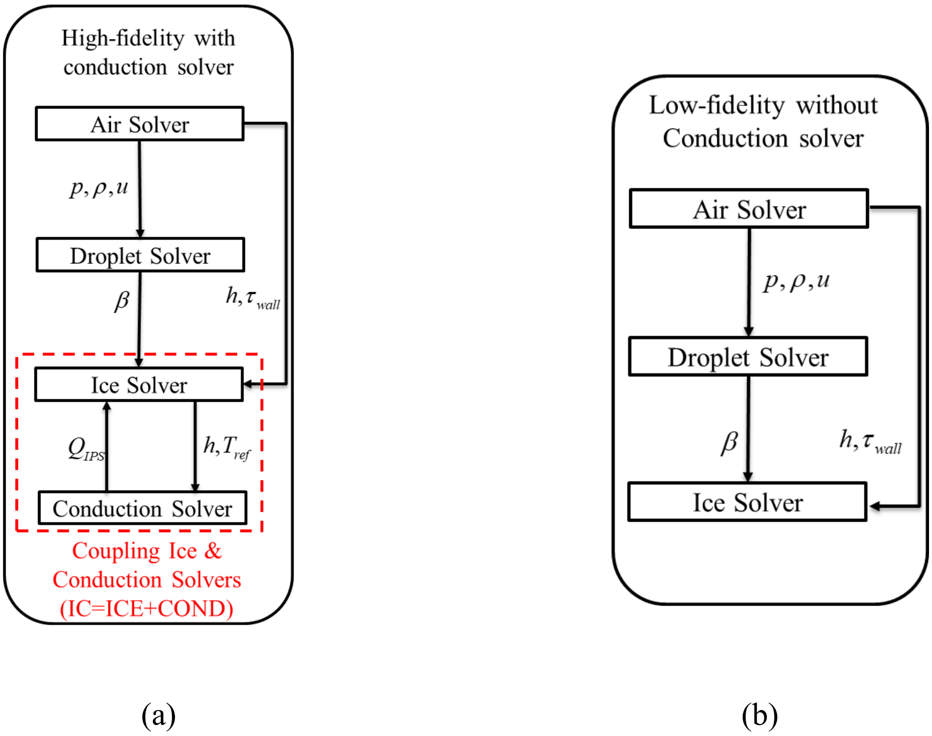


**Fig. 1.** Flowcharts of the ETIPS solvers: (a) high-fidelity with conduction and (b) low-fidelity without conduction.

### 2.1. High-fidelity numerical simulation

In this subsection, we detail the high-fidelity numerical simulation, which is broken down into its constituent solvers. The high-fidelity CFD framework integrates four interconnected solvers: airflow, droplet impingement, ice accretion, and conduction, enabling accurate modeling of ETIPSs with conjugate heat transfer (CHT) capabilities [5, 14].

As illustrated in Fig. 1, the air solver first provides the flow field parameters $(p, \rho, \boldsymbol{u})$ to the droplet solver, which computes droplet collection efficiency $(\beta)$ and heat transfer coefficients $(h,\ \boldsymbol{\tau}_{wall})$ at the surface. These outputs are subsequently fed into the ice solver to predict ice growth while accounting for local heat transfer and reference temperatures $(T_{ref})$. The conduction solver, coupled with the ice solver, incorporates the heat input from the solid $(Q_{IPS})$, enabling the calculation of the internal temperature distribution within the structure. This integrated approach ensures the accurate representation of aerodynamic, thermodynamic, and phase-change phenomena necessary for analyzing and optimizing anti-icing system performance under realistic icing conditions. Each of these solvers is described in further detail in the subsequent subsections, which also outline their specific methodologies and governing equations to comprehensively model IPSs.

### 2.1.1. Airflow solver

To simulate the airflow field, a finite volume method (FVM) is employed to solve the compressible NSF equations, which govern the conservation of mass, momentum, and energy, as follows:

$$\begin{bmatrix} \rho_a \\ \rho_a \boldsymbol{u}_a \\ \rho_a E \end{bmatrix}_t + \nabla \cdot \begin{bmatrix} \rho_a \boldsymbol{u}_a \\ \rho_a \boldsymbol{u}_a \boldsymbol{u}_a + p\boldsymbol{I} \\ (\rho_a E + p)\boldsymbol{u}_a \end{bmatrix} = \nabla \cdot \begin{bmatrix} 0 \\ \boldsymbol{\tau} \\ \boldsymbol{\tau} \cdot \boldsymbol{u}_a + \boldsymbol{Q} \end{bmatrix}, \tag{1}$$

$$\boldsymbol{\tau} = 2\mu[\nabla \boldsymbol{u}_a]^{(2)}, \ \boldsymbol{Q} = k\nabla T, \ E = h - \frac{p}{\rho_a} + \frac{\boldsymbol{u}_a \cdot \boldsymbol{u}_a}{2}, \tag{2}$$

where $\boldsymbol{\tau}$ and $\boldsymbol{Q}$ denote the non-conserved variables corresponding to viscous shear stress and heat flux, respectively. $[\nabla \boldsymbol{u}_a]^{(2)}$ stands for the traceless symmetric part of $\nabla \boldsymbol{u}_a$. Also, $E$ represents the total energy density. The ideal equation of state $p = \rho_g RT$ and the linear Navier-Stokes and Fourier laws (2) are employed to close the conservation laws (1).

The computational solver is parallelized using the Message Passing Interface (MPI) library, enabling efficient computation for unsteady simulations with high spatial and temporal resolution [34]. The time step of the air solver is selected based on standard CFL-type stability criteria, ensuring numerical stability of the advective and transport processes. Additionally, Roe's approximate Riemann solver is employed and enhanced to high-order accuracy using a least-squares reconstruction method in conjunction with Venkatakrishnan's limiter. To model turbulent viscous flow, the Spalart–Allmaras turbulence model is applied due to its simplicity and proven reliability in external aerodynamic simulations [5].

### 2.1.2. Droplet impingement solver

The droplet impingement solver models the air-droplet mixture flow field in the vicinity of the aircraft. Since water droplets have a negligible influence on the surrounding airflow, a one-way coupling strategy is employed, wherein the airflow influences droplet motion, but not vice versa. In practical icing simulations, the distribution of droplet sizes within clouds is typically characterized using the median volume diameter (MVD), which provides a simplified yet effective representation for estimating ice accretion [35].

The current solver is an Eulerian-based model for solving shallow water-type droplet equations (SWDEs). The original SWDE equations are not strictly hyperbolic. This issue was resolved in previous work by splitting the system into a source term and a well-posed part as follows [36]:

$$\begin{bmatrix} \rho \\ \rho \boldsymbol{u} \end{bmatrix}_t + \nabla \cdot \begin{bmatrix} \rho \boldsymbol{u} \\ \rho \boldsymbol{u}\boldsymbol{u} + \rho g d \boldsymbol{I} \end{bmatrix} = \begin{bmatrix} 0 \\ A_{\mathbf{u}}\left(\boldsymbol{u}_a - \boldsymbol{u}\right) + \boldsymbol{S}_b + \nabla \cdot \left(\rho g d \boldsymbol{I}\right) \end{bmatrix}. \tag{3}$$

The time step of the droplet solver is selected based on a standard CFL-type condition. The air and droplet velocity components are represented by $\boldsymbol{u}$ and $\boldsymbol{u}_a$, respectively. $\boldsymbol{S}_b$ is an estimation of the gravity and buoyancy forces on the droplet. The aerodynamic drag on droplets due to the airflow is represented by the term $A_{\mathbf{u}}(\boldsymbol{u}_a - \boldsymbol{u})$. Finally, the term $\nabla \cdot (\rho g d \boldsymbol{I})$ is added to both sides of the momentum equation to resolve the non-strictly hyperbolic nature of the Eulerian droplet equations [36].

### 2.1.3. Ice accretion solver

The ice accretion solver is a PDE-based thermodynamic model that solves mass and energy conservation equations for runback water on the surface. Unlike the algebraic Messinger model, this PDE-based formulation captures the dynamic evolution of mass and energy over time. During anti-icing simulations, there is no geometric deformation of the wing, as ice is prevented from forming on protected surfaces. The model is developed under the lubrication theory assumption, justified by the extremely thin water film typically observed in aircraft icing conditions, which is on the order of 10 μm. The ice solver calculates the equilibrium temperature ($T_{equi}$), water film thickness ($h_f$), and ice accretion rate ($\dot{m}_{ice}$) by solving the governing equations as follows [37]:

$$\begin{bmatrix} h_f \\ h_f T_{equi} \end{bmatrix}_t + \nabla \cdot \begin{bmatrix} \dfrac{h_f^2}{2\mu_w}\boldsymbol{\tau}_{wall} \\ \dfrac{h_f^2 T_{equi}}{2\mu_w}\boldsymbol{\tau}_{wall} \end{bmatrix} = \begin{bmatrix} \dfrac{S_M}{\rho_w} \\ \dfrac{S_E}{\rho_w c_{p,w}} + \dfrac{T_C S_M}{\rho_w} \end{bmatrix}, \tag{4}$$

$$S_M = \dot{m}_{imp} - \dot{m}_{evap} - \dot{m}_{ice},$$

$$S_E = \left[ Cp_w \tilde{T}_{d,\infty} + \frac{\|\boldsymbol{u}_d\|^2}{2} \right] \times \dot{m}_{imp} - L_{evap}\dot{m}_{evap} + h_c\left(T_{equi} - T_\infty\right) + \dot{m}_{ice}\left[L_{fus} - Cp_{ice}T_{equi}\right] + \dot{Q}_{IPS}, \tag{5}$$

$$\dot{m}_{imp} = U_\infty LWC_\infty \beta.$$

Here $\dot{m}_{imp}$ and $\dot{m}_{evap}$ are the instantaneous water droplet impingement mass and evaporation mass, respectively. Here, wall shear stress ($\boldsymbol{\tau}_{wall}$) and the convective heat transfer coefficient ($h_c$) are calculated in the air solver, while collection efficiency ($\beta$) and droplet impact velocity ($\boldsymbol{u}_d$) are predicted in the droplet solver, and finally, heat flux ($\dot{Q}_{IPS}$) from the solid is estimated in the conduction solver. The time step of the ice accretion solver is selected based on CFL-type stability constraints associated with water-film advection and thermal diffusion, ensuring stable and physically consistent temporal evolution of the water film and ice accretion rate.

### 2.1.4. Heat conduction solver

A finite volume-based heat conduction solver is developed to compute the temperature distribution within and across the surface of a multilayer composite structure. The governing energy equation is expressed as:

$$\rho_s C_{p_s} \frac{\partial T}{\partial t} = \nabla \cdot (k_s \nabla T) + S(t), \tag{6}$$

where $\rho_s$ , $C_{p_s}$ and $k_s$ are the density, specific heat, and thermal conductivities of each composite layer. Heater pads are placed between the composite layers, and $S(t)$ represents the transient heater fluxes. The conduction-solver time step is restricted by the explicit diffusion stability limit, determined by the thermal diffusivity and the minimum spatial grid size.

### 2.1.5. Coupling solvers using the tight conjugate heat transfer method

To accurately capture the strong thermal interaction at the fluid–solid interface, a tightly coupled strategy is adopted in this study (Fig. 2a). Within each coupling interval $\Delta t_{CHT}$, sub-iterations are performed between the ice and conduction solvers to enforce continuity of temperature and heat flux at the interface. This approach preserves second-order temporal accuracy and enhances numerical robustness. In contrast, a loosely coupled strategy exchanges interface information only once per coupling interval (Fig. 2b), resulting in first-order temporal accuracy and requiring a smaller $\Delta t_{CHT}$ to maintain numerical stability.

Convergence of the tightly coupled ice-conduction solver is evaluated by monitoring the surface temperature between successive sub-iterations over the ice domain. The $L^{\infty}$ norm is computed using the difference between the values obtained in the current and previous sub-iterations. Sub-iterations are terminated once the maximum change falls below a prescribed tolerance.

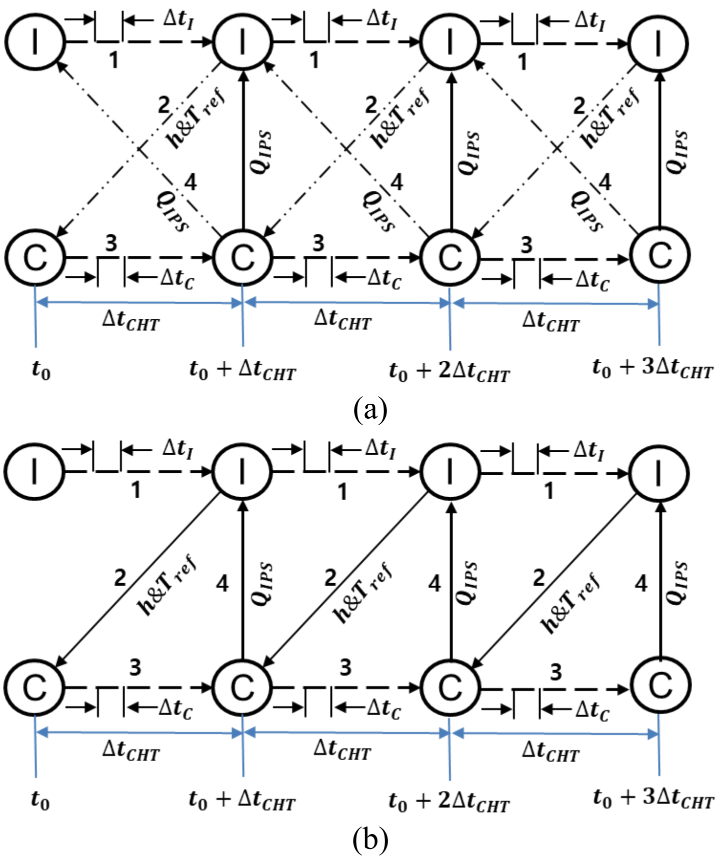


Fig. 2. Elaborate flowchart of (a) the tightly coupled, and (b) the loosely coupled approach for ice (I) and conduction (C) solvers.

In addition to the coupling strategy at the interface, special care is required in defining interface thermal boundary conditions. At the interface of the solid and ice domain, the mixed boundary condition with $h$ and $T_{ref}$ was applied to the conduction solver, and $Q_{IPS}$ was implemented as a source term to the energy conservation equation of the ice solver. In the ice solver, $T_{ref}$ was calculated as follows [38],

$$T_{ref} = T_{equi} - \frac{Q_{IPS}}{h}, \tag{7}$$

Here, $T_{equi}$ denotes the equilibrium interface temperature computed in the ice solver, and $Q_{IPS}$ is the heat flux obtained from the conduction solver. The value of $h$ does not influence the final physical solution; rather, it controls the convergence behavior of the CHT sub-iterations. Smaller values of $h$ typically accelerate convergence but may introduce numerical instability, whereas larger values improve stability at the cost of additional computational time. Accordingly, $h = 100$ is selected in this study as a practical compromise between stability and efficiency [38]. The reference temperature $T_{ref}$ and the heat transfer coefficient $h$ are communicated to the conduction solver as a mixed boundary condition, and the resulting heat flux is evaluated using $h$, $T_{ref}$, and the local wall temperature from the conduction solver $T_{cond}$ as follows [38]:

$$Q_{IPS} = h(T_{cond} - T_{ref}). \tag{8}$$

### 2.2. Low-fidelity numerical simulation

In the low-fidelity simulations, we use a simplified set of solvers for airflow, droplet impingement, and ice accretion solvers, as illustrated in Fig. 1(b). Unlike the high-fidelity solver, which includes conjugate heat transfer and a conduction solver for realistic thermal modeling, the low-fidelity model excludes heat conduction in composite layers. Instead, we directly impose heat sources and define heater pad lengths within the protection zone to represent the ETIPS. This simplification enables rapid evaluation, which reduces computational cost from the approximately 1,444 minutes required for a high-fidelity solver simulation to just 3 minutes for the low-fidelity ICE solver.

While less accurate, this low-fidelity approach is ideal for multi-fidelity frameworks. Its low computational cost makes it possible to generate numerous samples. These samples effectively train machine learning models when combined with a limited number of high-fidelity simulations. Accordingly, this strategy achieves accuracy that is comparable to using many high-fidelity samples, while significantly cutting computational demand and simplifying the multi-fidelity Gaussian process regression (MFGPR) model structures.

## 3. Multi-fidelity surrogate optimization (MFSO) methodology

In this study, we propose a novel algorithm for analyzing ETIPS based on a multi-fidelity surrogate-based optimization strategy, as illustrated in Fig. 3. The methodology is initiated by generating an initial set of heater power density samples (design variables) via Latin hypercube sampling (LHS). This is followed by high and low fidelity simulations, by changing the heater power densities at fixed icing and flow conditions. Since icing and flow conditions are fixed, the air and droplet solvers are executed only once for all samples. For the high-fidelity solver, the ice and conduction solvers are dynamically updated, while in the low-fidelity solver, only the ice solver is updated. This setup allows the heater power density to vary in each sample, enabling the simulation of ice accretion and thermal response under different operational conditions.

The simulation results for high- and low-fidelity cases are stored in separate databases. To reduce the dimensionality of the data, proper orthogonal decomposition (POD) is applied, and the resulting POD coefficients—representing key physical features such as maximum ice growth, end film height, and target wall temperature—are used as the outputs for training an MFGPR surrogate model, with heater power density as the input. Once trained, this surrogate model enables rapid prediction of system behavior.

The final stage involves optimization using the MADS algorithm within the nonlinear optimization by mesh adaptive direct search (NOMAD) software [36] to iteratively determine the optimal heater power density configuration. This optimization aims to minimize total electrical power consumption while meeting physical constraints related to ice growth and thermal performance. The proposed framework thus provides an efficient and accurate method for designing and evaluating ETIPS under realistic icing scenarios.

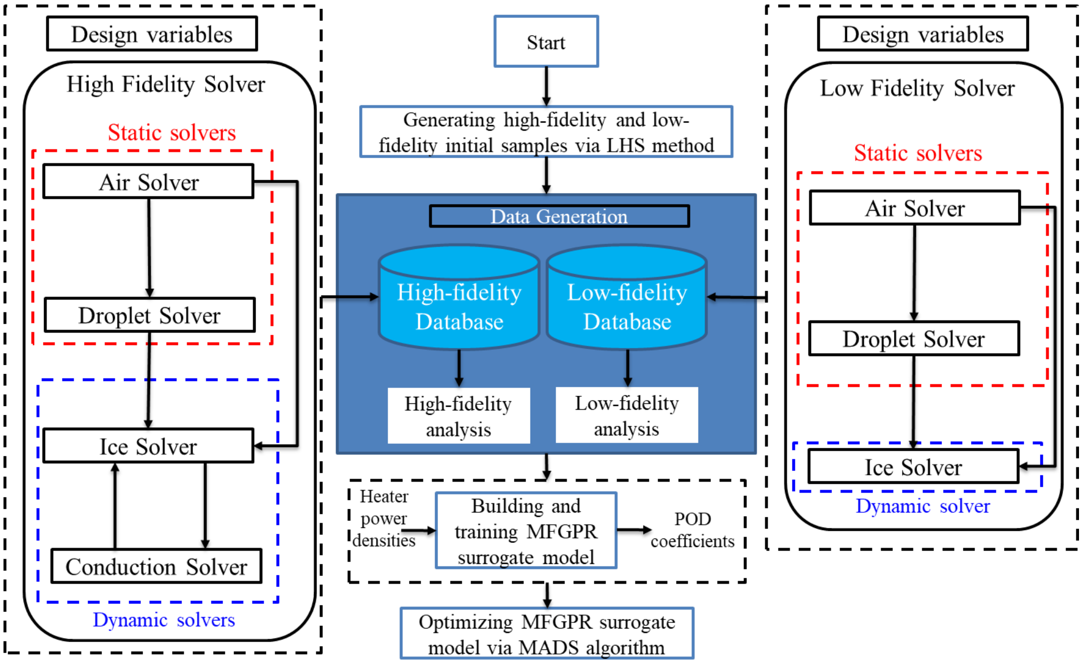


**Fig. 3.** Framework and workflow of the multi-fidelity surrogate modeling strategy for electrothermal anti-icing system analysis.

### 3.1. Multi-fidelity surrogate model (MFSM)

Figure 4 presents the integrated framework developed for multi-fidelity surrogate modeling of the ETIPS. The workflow begins with the generation of heater power density samples (design variables) using LHS, a space-filling design strategy that ensures comprehensive coverage of the input domain. These samples are then processed through the high-fidelity and low-fidelity simulations, and the resulting output data is subsequently arranged into a structured data matrix. POD is employed to extract the dominant spatial and temporal modes, thereby reducing the dimensionality of the system response and yielding a compact set of POD coefficients that effectively capture the essential dynamics.

These coefficients are used as target outputs for training MFGPR surrogate models. The models are trained using heater power density samples generated via LHS as inputs, enabling rapid and accurate prediction of system performance. To ensure model reliability and to guide optimal sampling, an evaluation module is employed, featuring leave-one-out cross-validation

(LOOCV) for accuracy assessment, alongside self-organizing map (SOM) and K-means clustering for intelligent sample point selection. The resulting train-test framework predicts key performance metrics, including temperature distribution, ice accretion mass, and water film thickness, allowing for the efficient evaluation of novel heater configurations without the need for repeated computationally expensive high-fidelity and low-fidelity simulations. This approach substantially reduces computational cost while preserving the high-fidelity predictions that are critical for effective anti-icing system design.

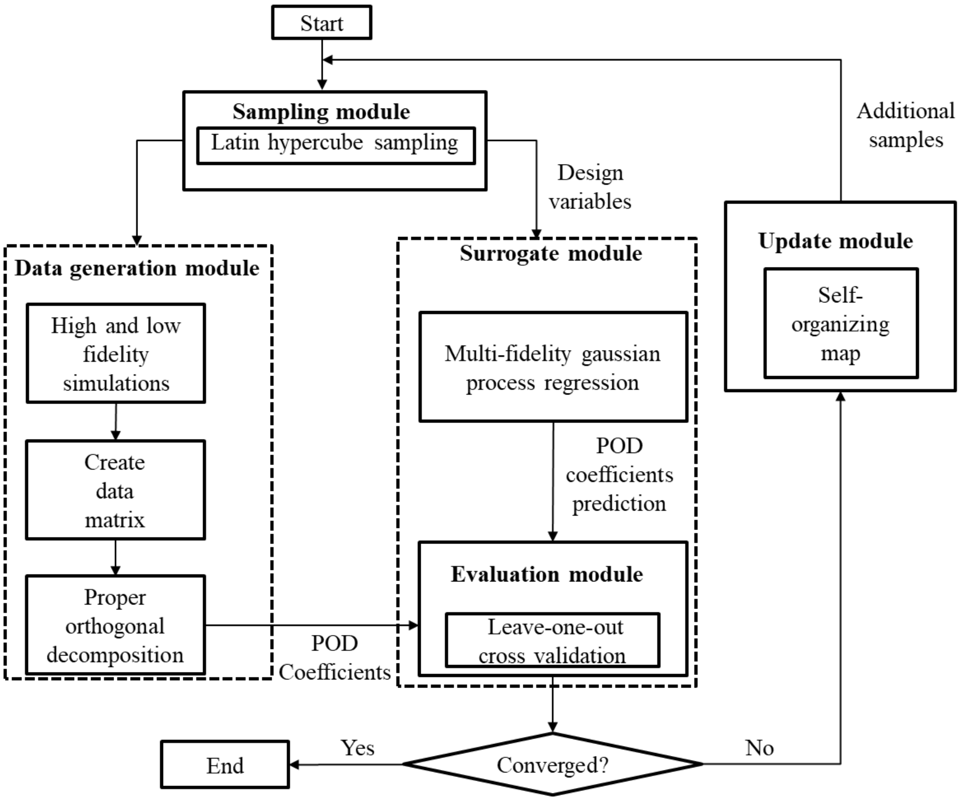


**Fig. 4.** MFSM development workflow for the electrothermal anti-icing system using POD-MFGPR, LOOCV, and self-organizing map.

### 3.1.1. Latin hypercube sampling (LHS)

In this investigation, we used the LHS statistical method because it can be used to efficiently explore multi-dimensional input spaces, particularly in our case, where we have seven inputs, that is, the heater power density of each pad. By dividing its cumulative distribution into *n* equally probable intervals and sampling once from each interval, it ensures that each input variable is sampled evenly across its range. Unlike simple random sampling, which may result in clustering and poor space-filling, LHS guarantees stratification along each dimension, making it more effective at capturing variability with fewer samples.

Mathematically, LHS draws samples from a *d*-dimensional space such that the sample matrix $\mathrm{X} \in \mathbb{R}^{n \times d}$ satisfies the condition that each column contains a permutation of the set $\left\{ \frac{1}{n}, \frac{2}{n}, \frac{3}{n}, \ldots, \frac{n}{n} \right\}$ (after transformation through inverse cumulative distribution functions for non-uniform distributions [39]. LHS is widely used in surrogate modeling, sensitivity analysis, and reliability engineering.

### 3.1.2. Proper orthogonal decomposition (POD)

Performing the POD procedure for a surrogate model provides an optimal orthonormal set of basis vectors for a given ensemble of data [40-43]. The objective is to yield a set of basis vectors, Φ, of length *n* for an ensemble of data, $Y = \{Y_1, Y_2, \ldots, Y_N\}$ , where $Y_i = \{y_{i1}, y_{i2}, \ldots, y_{im}\}$. For continuous spaces, *N* can be very large, and the solution of the corresponding eigenvalue problem can be prohibitively expensive. To avoid this problem, instead of solving an *n* × *n* matrix for the eigensystem, Sirovich [25] introduced the method of snapshots (an *N* × *N* matrix, where *N* is the number of snapshots in the ensemble of data). The POD basis modes are written in terms of the members of the ensemble data and the eigenvector of the correlation matrix

$$C_{ij} = \frac{1}{N} Y_i^T Y_j ,$$

$$\Phi_i = \sum_{i=1}^{N} v_i Y_i, \tag{9}$$

where $v_i$ is the eigenvector of the correlation matrix. Among all POD basis modes, only M number of available modes are chosen by energy level. Then, a surrogate model with a reduced subspace defined by an energy level, $Y^{POD} = (\Phi_1, \Phi_2, ..., \Phi_M)$, can be obtained,

$$Y^{POD} = \sum_{i=1}^{M} a_i' \Phi_i, \tag{10}$$

where $a_i'$ represents the POD, coefficient defined as $\frac{y_i \Phi_i}{\Phi_j \Phi_i}$, $\Phi_i$ represents the ith POD basis mode, and M indicates the truncation of the expansion at the desired level of energy content. The fraction of the total energy associated with each mode, $\Phi_i$, can be computed,

$$E = \sum_{j=1}^{M} \lambda_j \Big/ \sum_{i=1}^{Ns} \lambda_i, \tag{11}$$

where λ, *Ns* denote an eigenvalue and the total number of snapshots, respectively. When considering the POD for the present problem, the CFD solutions at grid points and the corresponding icing conditions can be treated as Y and N, respectively.

### 3.1.3. Multi-fidelity Gaussian process regression (MFGPR)

Gaussian process regression (GPR) is a nonlinear, non-parametric Bayesian approach that offers a powerful solution to regression problems, especially when dealing with small sample sizes [44-47]. Given a dataset $D = (X, Y) = \left\{ (x^{(i)}, y^{(i)}) \in \chi \times y \subset \mathbb{R}^d \times \mathbb{R} \mid i = 1, ..., N_{data} \right\}$, where $X = \left[ x^{(1)} | ... | x^{(N_{data})} \right]$ denotes the input matrix and $Y = \left[ y^{(1)}, ..., y^{(N_{data})} \right]^T$ represents the corresponding output vector. The objective is to construct a regression model $f : \chi \to y$ capable of capturing the underlying relationship between the d-dimensional inputs and the scalar response [48]. To quantify the uncertainty in selecting among potentially many plausible functions that fit the data, a Gaussian Process (GP) prior is employed [49]. A GP is fully defined by a mean function $m(x)$ and a covariance kernel $\kappa(x, x')$, such that [50]:

$$f(x) \sim GP(m(x), \kappa(x, x')). \tag{12}$$

Given the nature of the problem, the optimal kernel structure in GPR is inherently problem-specific and requires careful selection before tuning the associated hyperparameters. To address this, we developed a shell script to systematically evaluate thousands of kernel structures, each with varying hyperparameter configurations. The objective was to identify the kernel structure that yielded the highest coefficient of determination ($R^2$) on both training and testing datasets, while minimizing the relative root mean square error (RMSE) between them. Ultimately, the composite kernel employed in this study consisted of the sum of a scaled Matérn kernel and a white noise kernel, which proved effective for the given regression task,

$$\kappa(x, x') = C.k_{Matern}(x, x'; \ell, \upsilon) + \sigma_n^2 \delta_{x,x'}. \tag{13}$$

The Matérn kernel with smoothness parameter $\upsilon = 2.5$ is defined as [36]:

$$k_{Matern}(x, x') = \left(1 + \frac{\sqrt{5}r}{\ell} + \frac{5r^2}{3\ell^2}\right)\exp\left(-\frac{\sqrt{5}r}{\ell}\right) \tag{14}$$

where $r = \|x - x'\|$, $C = 1.0$ is the characteristic length scale, and $\ell$=1.0 denotes the constant kernel, which controls the overall signal variance. The Matérn kernel with $\upsilon = 2.5$ guarantees twice differentiable sample paths, striking a desirable balance between smoothness and model flexibility. To account for observation noise, a white noise kernel that models unstructured variability was incorporated. This composite kernel structure, comprising the Matérn, constant, and white noise components, enables the Gaussian process to capture both the underlying trends and stochastic disturbances present in the data.

To identify the optimal set of hyperparameters, we employed the GridSearchCV tool available in Scikit-learn, utilizing 10-fold cross-validation to ensure robust model evaluation. To maximize the log-marginal likelihood and effectively search for the best hyperparameters, we adopted the L-BFGS-B algorithm—a quasi-Newton method suitable for constrained optimization of the log-marginal likelihood. The number of estimators (*n* estimators) was set to 20 to iterate over each output individually, enabling the selection of optimal hyperparameters for each target dimension. Furthermore, to guarantee numerical stability and consistent scaling across input features, standard preprocessing techniques such as min-max normalization were applied.

We enhanced this foundational GPR approach by using a multi-fidelity surrogate modeling strategy. Rather than relying solely on expensive, high-fidelity models, this method incorporates cheaper, lower-fidelity models that are correlated with the accurate ones. The foundational formulation, known as co-kriging, models the expensive high-fidelity output ($f_h(x)$) as a combination of the cheap low-fidelity function ($f_l(x)$) scaled by a parameter ($\rho$) and a discrepancy between the two models ($\delta(x)$). In the widely used auto-regressive co-kriging formulation, this is expressed as: $f_h(x) = \rho f_l(x) + \delta(x)$ This structured correlation enables the construction of an accurate surrogate for the high-fidelity model using a relatively small number of high-fidelity samples, significantly reducing computational cost without compromising prediction accuracy.

It is worth mentioning that while the high-fidelity and low-fidelity kernel structures are the same, the hyperparameters for each fidelity should be tuned separately before going through the multi-fidelity approach. All components of this MFSM were implemented using the open-source Python library, Scikit-learn.

#### 3.1.4. Leave-one-out cross-validation (LOOCV)

The accuracy of the surrogate model was assessed by direct comparison with full-order CFD solutions using an LOOCV approach [51]. In a dataset consisting of $N_s$ snapshots obtained from CFD simulations, one snapshot is iteratively designated as the reference solution, while the remaining $N_s$-1 snapshots are used to construct the surrogate model. The surrogate model is then evaluated under the conditions corresponding to the reference snapshot, and the resulting prediction is compared with the actual CFD solution at that point. The error between the surrogate model and the CFD prediction is quantified, and this procedure is repeated for each snapshot in the dataset, ensuring that the surrogate model is validated across the entire parametric domain.

Notably, LOOCV does not require any additional data samples beyond those already available, making the computational cost of validation equivalent to that of constructing the surrogate model using $N_s$ snapshots. Furthermore, this approach is computationally efficient, as each model constructed with $N_s$-1 snapshots is independent and thus amenable to parallelization.

In this study, the primary quantities of interest are the mass of ice accumulated on the surface, the target wall temperature, and the height of the water film at the end of the protection limit under the anti-icing mode of the ETIPS. The accuracy of the surrogate model is assessed by calculating the maximum deviation between the surrogate predictions and the corresponding CFD results at each grid point along the anti-icing surface. To ensure adequate model performance and convergence, the number of snapshots is incrementally increased during the iterative training process until the error reaches an acceptable threshold and the model demonstrates reliable predictive capability.

#### 3.1.5. Self-organized map (SOM)

In the design of experiments, establishing an adequately rich set of snapshots within the parametric space is critical, as it directly influences the accuracy and generalizability of the surrogate models. While error metrics computed by evaluation modules offer insights into the distribution of errors across selected samples, they provide limited guidance for regions of the parametric space not yet explored. This raises essential questions regarding the number of additional samples required and their optimal placement within the parameter domain.

To address this challenge, an effective sampling strategy is needed to guide the selection of new samples. For this purpose, clustering methods that capture the interactions between input and output variables can be instrumental in both identifying informative sample locations and enhancing system understanding.

In the present study, a SOM [52] was utilized to cluster the error distributions and inform the placement of additional samples. The SOM, a type of neural network based on unsupervised and competitive learning [53], generates a topology-preserving mapping from high-dimensional input space to a typically two-dimensional lattice of neurons. This property enables the SOM to function effectively as a clustering tool for high-dimensional data. Within the SOM framework, new sample points are selected using the k-means clustering algorithm, and the sampling procedure is iteratively applied until the maximum observed error falls below a predefined threshold.

### 3.2. Optimization problem formulation and solution

As shown in the flowchart in Fig. 3, the final stage of the methodology involves an optimization loop. This loop utilizes our MFSM to efficiently find the optimal heater power configuration. The primary goal is to minimize the total electric power consumed by the system. This is crucial to maximize energy efficiency and reduce operational costs. Simultaneously, the optimization ensures the anti-icing system operates effectively and safely. This is accomplished by adhering to specific physical constraints, such as limits on ice growth and surface temperature. The MADS algorithm is employed within this framework to guide the iterative search for the optimal solution.

#### 3.2.1. Problem formulation and constraints

As illustrated in the flowchart in Fig. 5, the algorithm commences with building a multi-fidelity surrogate model, then proceeds to define the objective and constraint functions. Careful and intelligent selection of these functions is essential, particularly due to the limitations of the ETIPS, which is known to be energy-intensive. Therefore, we select the total electric power,

$$\int_{s_{el}}^{s_{eu}} P''(s)ds\,, \tag{15}$$

as the objective function to minimize the overall power density of all heater pads during the multi-fidelity surrogate-based optimization process. Here, $P''(s)$ is power density, $s$ represents the spanwise coordinate along the heated surface, $s_{eu}$ and $s_{el}$ denote the upper and lower bounds of the protection region, respectively. This approach ensures flight safety while identifying the optimal configuration of each heater pad [19]. The definition of constraints is regime-dependent; that is, constraints vary depending on whether the system is operating in the running-wet or evaporative regime.

For the running-wet regime, we define two different constraints: maximum ice growth and target wall temperature. In maximum ice growth, the constraint is defined as $\max\{\dot{m}''_{ice}(s)\}_{S_{el}}^{S_{eu}}$ , where $\dot{m}''_{ice}$ is the rate of mass of ice. The constraint for target wall temperature is defined as $\int_{s_{el}}^{s_{eu}} |T_0(s) - T(s)| ds$, where $T_0$ is the target wall temperature and $T(s)$ is the wall temperature distribution. In this study, we compared the results of the target wall temperature constraint for different $T_0$ values, including $273.2^{\circ}$K, $274^{\circ}$K, $275^{\circ}$K, $276^{\circ}$K, $278^{\circ}$K, $280^{\circ}$K. For the evaporative regime, we incorporated the end film height constraint as $h_f(s_{el}) + h_f(s_{eu})$, where $h_f(s_{el})$ and $h_f(s_{eu})$ are the water film height at the end of the heating zone on the lower and the upper surfaces, respectively. The end film height constraint ensures that the water film completely evaporates before it reaches the protection limits [19].

Once the objective and constraints are defined, the algorithm checks whether the stopping criteria—specific to each regime—have been satisfied. If they are met, the optimal configuration is obtained. Otherwise, the process proceeds with the NOMAD software, which applies the MADS algorithm to generate a new set of design variables (heater power densities). These variables are evaluated using the surrogate model, and the updated results are then used to reassess the objective and constraints. The procedure iterates in this manner until convergence is reached.

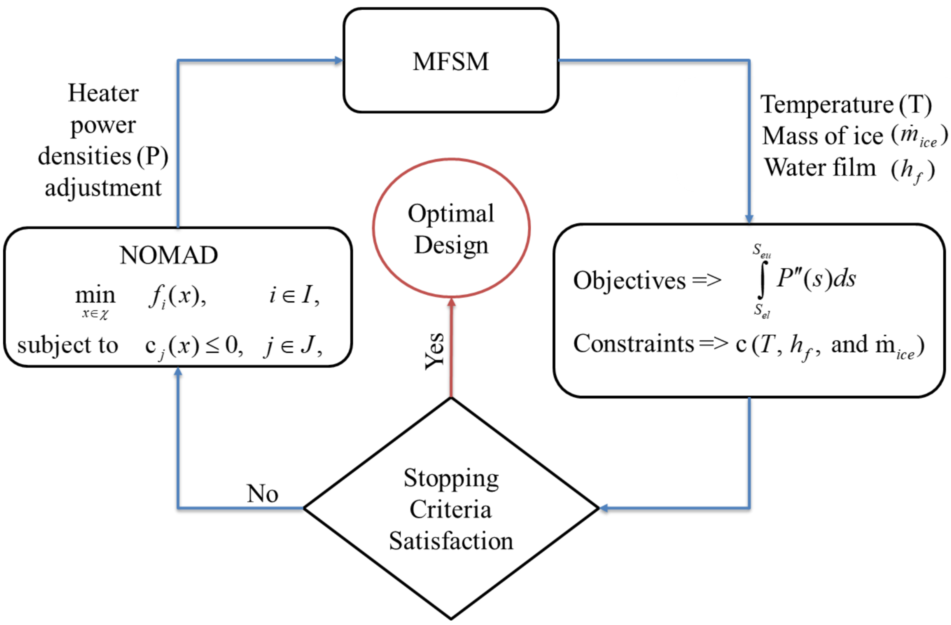


**Fig. 5.** Optimization workflow for the heater power density of each pad using the multi-fidelity surrogate model (MFSM)-based NOMAD framework.

We employed the MADS algorithm to optimize our objective function by identifying its minimum value. The following summary provides a brief overview of MADS, focusing on its definition, the rationale for its application in this study, and its primary advantages. A comprehensive and detailed explanation of the algorithm lies beyond the scope of this study; for an in-depth understanding, we recommend consulting the seminal work by Audet et al. [18, 54], who pioneered the development of MADS.

### 3.2.2. Mesh adaptive direct search (MADS) algorithm

MADS is a derivative-free optimization algorithm designed for constrained and black-box problems where gradients are unavailable or unreliable. MADS belongs to the class of direct search methods and improves upon traditional pattern search algorithms by using an adaptive mesh that refines the search granularity as iterations progress. At each iteration, the method explores the objective function through a set of trial points generated on a mesh, using a pair of steps: a poll step and an optional search step. The poll step ensures convergence by evaluating nearby points in directions that form a positive spanning set, while the search step allows the incorporation of heuristics or surrogate models to improve exploration.

NOMAD (Nonlinear Optimization by Mesh Adaptive Direct Search) is a robust, open-source software implementation of the MADS algorithm [55]. Developed in C++, NOMAD supports various problem classes, including continuous, integer, and mixed-variable optimization with linear and nonlinear constraints. It has been applied in numerous engineering disciplines, notably in aerospace design, structural optimization, and energy systems, where evaluating the objective function involves expensive simulations. NOMAD allows integration with black-box solvers, surrogate models, and parallel evaluations, making it suitable for large-scale and industrial applications. Its theoretical foundation and practical effectiveness have been extensively validated in the optimization community [55].

## 4. Results and discussion

This section presents the comprehensive results of this study, highlighting the efficacy and efficiency of the multi-fidelity surrogate-based optimization approach for the electrothermal ice protection system for in-flight anti-icing. We begin by validating the high-fidelity computational setup against experimental data and detailing the strategic sampling methodology. Subsequently, the performance of the developed surrogate models is presented, culminating in the core results of the multi-fidelity optimization for both running-wet and evaporative anti-icing regimes.

### 4.1. High-fidelity computational setup validation and data generation

#### 4.1.1. High-fidelity computational setup validation

The experimental setup utilized a rectangular wing featuring a NACA0012 airfoil section and a chord length of 0.9144 meters. The wing's leading edge comprised a six-layer composite**,** integrating seven heating pads strategically placed between the composite layers. As depicted in Fig. 6, these heaters varied in length: Heater A was 19 mm, Heaters B, C, D, and E were 25.4 mm, and Heaters F and G measured 38.1 mm. Notably, all heaters were offset by 4.763 mm towards the airfoil's upper surface during manufacturing. The precise thickness and thermal properties for each layer of the leading-edge composite are detailed in Table 2.

**Table 2**

Material properties of the composite layers.

| Material | Thickness [mm] | $\rho$ [kg/m$^3$] | $k$ [W/m·K] | $C_p$ [J/Kg·K] |
|---|---|---|---|---|
| Heating Element | 0.013 (x1) | 8906.3 | 41 | 385 |
| Erosion Shield | 0.203 (x1) | 8025.3 | 16.3 | 502 |
| Elastomer | 0.280 (x2) | 1383.9 | 0.256 | 1260 |
| Fiberglass/Epoxy Composite | 0.890 (x1) | 1794.0 | 0.294 | 1570 |
| Silicon Foam Insulation | 3.430 (x1) | 648.8 | 0.121 | 1130 |

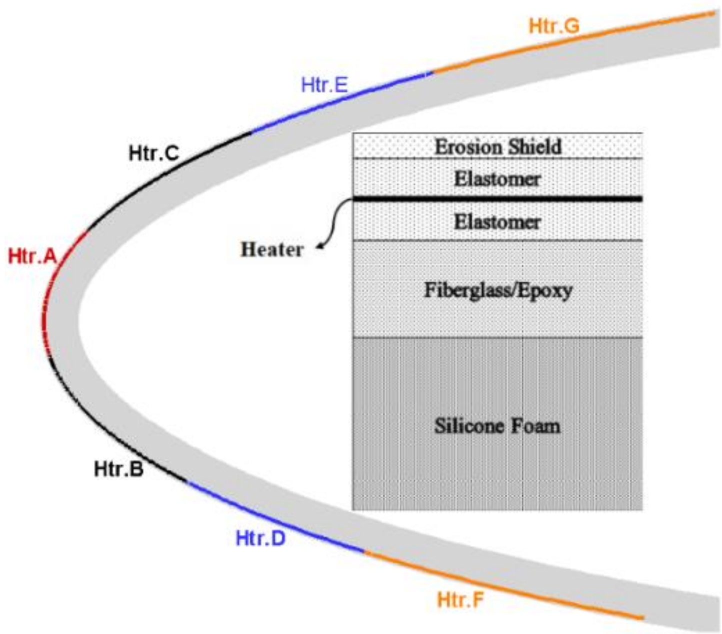


**Fig. 6.** Arrangement of heaters and cross-section of the leading edge.

The anti-icing and de-icing experiments conducted at the NASA Lewis Icing Research Tunnel (IRT) [56] utilized a consistent wing and IPS throughout the campaign. To ensure computational accuracy, a mesh independence study was performed across three grid sizes: medium (55,288/9,760 cells for air/solid domains), fine (121,473/18,920 cells for air/solid domains), and very fine (170,553/32,650 cells for air/solid domains). As depicted in Fig. 7, the wall temperature predictions from the fine grid closely aligned with those of the very fine grid, leading to the selection of the fine grid for all subsequent simulations.

Within the solid domain, the inner wall received a zero-heat flux boundary condition, indicating negligible heat transfer, whereas the outer wall used a conjugate heat transfer condition to capture thermal interactions with the runback water film.

From the NASA Lewis Icing Research Tunnel (IRT) experiments [56], two test cases were selected for solver validation, covering different anti-icing regimes, including evaporative and running-wet conditions. Table 3 summarizes the corresponding icing and flight conditions, together with the applied heater power densities. These validation cases are based on in-flight icing tests conducted in the NASA Lewis IRT [56] and represent in-flight environments, including free-stream velocity, temperature, liquid water content (LWC), and median volume diameter (MVD).

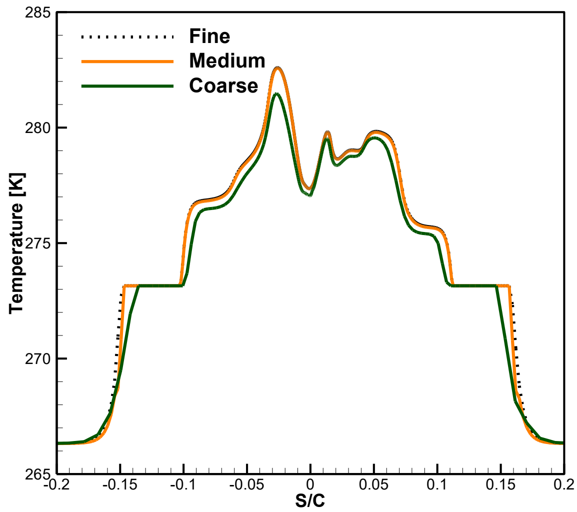


**Fig. 7.** Comparison of temperature profiles for different grids for case 22B.

The CHT coupling time step ( $\Delta t_{\mathrm{CHT}}$ ) specifies the frequency of information exchange between individual solvers during the anti-icing simulation [5, 6, 14]. To verify the independence of the computational results to $\Delta t_{\mathrm{CHT}}$, we conducted de-icing simulations with three different CHT time steps, of $\Delta t_{\mathrm{CHT}} = 0.01\mathrm{s}$ , $\Delta t_{\mathrm{CHT}} = 0.1\mathrm{s}$ , and $\Delta t_{\mathrm{CHT}} = 1.0\mathrm{s}$ . The temperature distributions obtained with 0.01s and 0.1s were essentially indistinguishable, whereas $\Delta t_{\mathrm{CHT}} = 1.0\mathrm{s}$ noticeably smoothed the local temperature peaks due to insufficient temporal resolution of the CHT sub-iterations. Because the difference between the 0.01s and 0.1s solutions was negligible, $\Delta t_{\mathrm{CHT}} = 0.1\mathrm{s}$ was adopted for all high-fidelity simulations. The effect of the CHT time-step size is illustrated in Fig. 8.

The total physical simulation time was determined by monitoring of wall temperature, water-film, and mass of ice variables until steady-state behavior was reached. Once the key quantities became time-invariant, the solution was deemed converged, indicating that the chosen simulation time was sufficient.

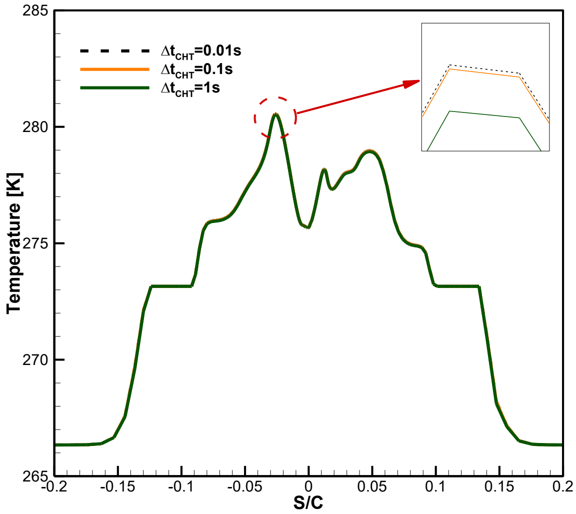


**Fig. 8.** Comparison of CHT time-step size on the predicted wall-temperature distribution along the normalized chord.

**Table 3**

Heater powers and icing conditions for the validation cases.

| variables | Case 22B | Case 22A |
|---|---|---|
| Heater A [W/m$^2$] | 4805 | 46500 |
| Heater B [W/m$^2$] | 4030 | 32550 |
| Heater C [W/m$^2$] | 2945 | 18600 |
| Heater D [W/m$^2$] | 2945 | 10230 |
| Heater E [W/m$^2$] | 3410 | 6975 |
| Heater F [W/m$^2$] | 2635 | 9920 |
| Heater G [W/m$^2$] | 2325 | 10230 |
| $T_\infty$ [K] | 265.5 | 265.5 |
| $U_\infty$ [m/s] | 44.7 | 44.7 |
| LWC [g/m$^3$] | 0.78 | 0.78 |
| MVD [μm] | 20 | 20 |

Figure 9 presents a comprehensive validation study comparing experimental measurements with two numerical prediction models across distinct thermal scenarios: the evaporative case (22A) and the running wet case (22B). The experimental data, represented by yellow circular markers, serve as the benchmark against which both the established "ANTICE [56]" model (shown as dashed red lines) and the newly developed “Present” model (solid black lines) were evaluated. The plots simultaneously track temperature distribution in Kelvin and heater power density in kW/m² along a non-dimensional chord position (S/C), while also delineating critical operational boundaries, including protection limits, impingement zones, and water film extent regions.

The validation results demonstrated that the present model exhibits superior predictive capability and showed notably closer alignment with experimental temperature profiles and thermal characteristics compared to the ANTICE [56] reference model across both test conditions. This enhanced agreement is particularly evident when capturing the complex thermal transitions and water film behavior, indicating that the present model provides a more accurate representation of the underlying physical phenomena governing heat transfer and fluid dynamics in both the evaporative and running wet operational regimes.

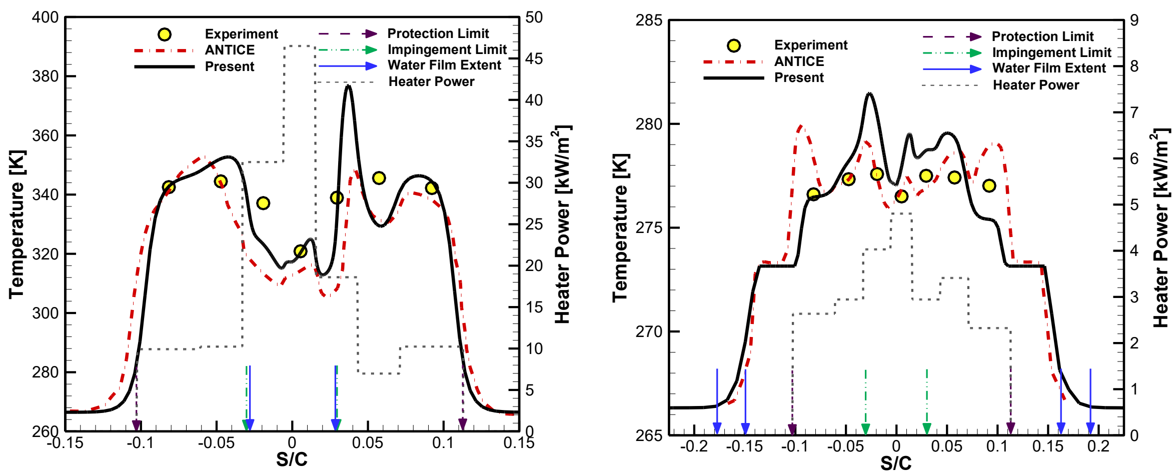


(a) (b)

**Fig. 9.** Validation of the present model with experimental and numerical temperature distributions for (a) case 22A (evaporative) and (b) case 22B (running wet).

Figure 10 presents a comparative analysis of temperature distributions along the protection limit for both the high-fidelity and low-fidelity simulations. All subplots correspond to the same ice and flight conditions as Case 22B in Table 3, while each represents a distinct heater power density. The exact heater power densities (in W/m²) for heaters A through G used in these simulations are listed in Table 4.

As shown in subplots (a) and (b) of Fig. 10, the low-fidelity simulation consistently predicts higher temperatures than the high-fidelity simulation. This systematic difference arises because the high-fidelity model includes detailed conduction algorithms, capturing heat dissipation through the composite material, whereas the low-fidelity model does not. Consequently, by reflecting the critical role of conductive heat transfer within the composite structure, the high-fidelity simulation produces lower, more realistic temperature values. These results highlight that including conduction effects in the computational model yields thermodynamically accurate and conservative predictions that better represent the actual thermal behavior of the system.

**Table 4**

Heater power densities (W/m²) for subplots in Fig. 10.

| Heater | Case A | Case B |
|---|---|---|
| A | 3732.56 | 4402.48 |
| B | 4402.31 | 4524.03 |
| C | 4215.08 | 3852.40 |
| D | 4800.48 | 4813.71 |
| E | 3658.48 | 2350.51 |
| F | 4863.87 | 2077.60 |
| G | 3139.72 | 3615.26 |

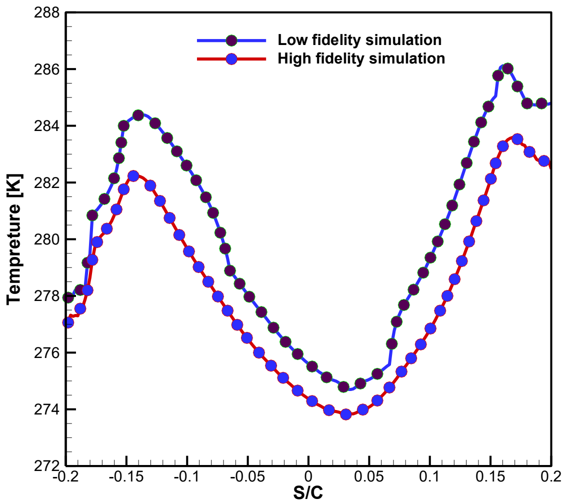


Case A

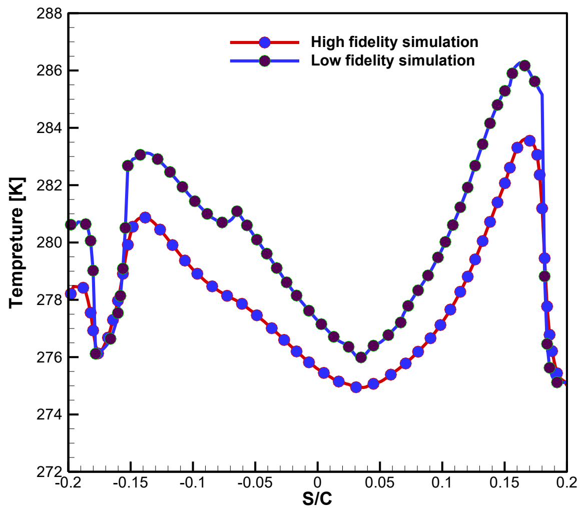


Case B

**Fig. 10.** Comparison of high- and low-fidelity simulations for temperature distribution along the protection limit under varying heater power densities.

### 4.1.2. Multi-fidelity data generation and sample size determination

To determine the appropriate number of samples for both the high-fidelity and low-fidelity datasets in a multi-fidelity design optimization framework, we refer to the guideline provided by Liu et al. [57], which ties the sample size to the number of design variables (D). In this study, we have 7 design variables. According to Liu et al. [57], the minimum required number of low-fidelity samples should be at least 10×D, while the minimum for high-fidelity simulations should be 5×D to 7×D. We used these criteria to establish the sampling strategy. To evaluate the predictive accuracy and performance of the developed models, three key metrics were utilized: the coefficient of determination ($R^2$), root mean squared error (RMSE), and normalized root mean squared error (NRMSE). The coefficient of determination, $R^2$, quantifies the proportion of the variance in the dependent variable that is predictable from the independent variables. It is formulated as:

$$R^2 = 1 - \frac{\sum_{i=1}^{N}(y_i - \hat{y}_i)^2}{\sum_{i=1}^{N}(y_i - \bar{y}_i)^2}, \tag{16}$$

where $y_i$ is the true value, $\hat{y}_i$ is the value predicted from the surrogate model, $\bar{y} = \frac{1}{N}\sum_{i=1}^{N} y_i$ represents the average of the true value, and $N$ is the total number of samples.

The RMSE provides a measure of the average magnitude of the errors, giving a higher weight to larger errors. It is calculated as:

$$RMSE = \sqrt{\frac{1}{N}\sum_{i=n}^{N}(y_i - \hat{y}_i)^2}, \tag{17}$$

where $y_i$ is the true value, $\hat{y}_i$ is the prediction value, and $N$ is the total number of samples. Finally, the NRMSE allows for a more direct comparison of model performance across different datasets or scales by normalizing the RMSE. It is defined as:

$$NRMSE = \frac{RMSE}{y_{\max} - y_{\min}}, \tag{18}$$

where $y_{\max}$ and $y_{\min}$ are the maximum and minimum true values in the dataset, respectively.

As illustrated in Fig. 11, the model performance metrics—RMSE, NRMSE, and $R^2$—show notable improvement as the sample size increases, particularly up to the recommended thresholds. Beyond these points, the improvements become marginal, suggesting that the selected sample sizes (400 for the high-fidelity model and 1,250 for the low-fidelity model) are both adequate and well-justified. This pattern is clearly demonstrated in Fig. 11, which shows the convergence behavior of the performance metrics. Specifically, Figs. 11(a), (b), and (c) present the RMSE, NRMSE, and $R^2$ values for the low-fidelity surrogate model, respectively, all indicating consistent improvement with larger sample sizes. Likewise, Figs. 11(d), (e), and (f) show the corresponding metrics for the high-fidelity surrogate model. The graphical trends align with the tabulated results, confirming that the chosen sample sizes are sufficient to achieve stable and accurate model performance for both fidelity levels, thereby supporting the effectiveness of the adopted sampling strategy.

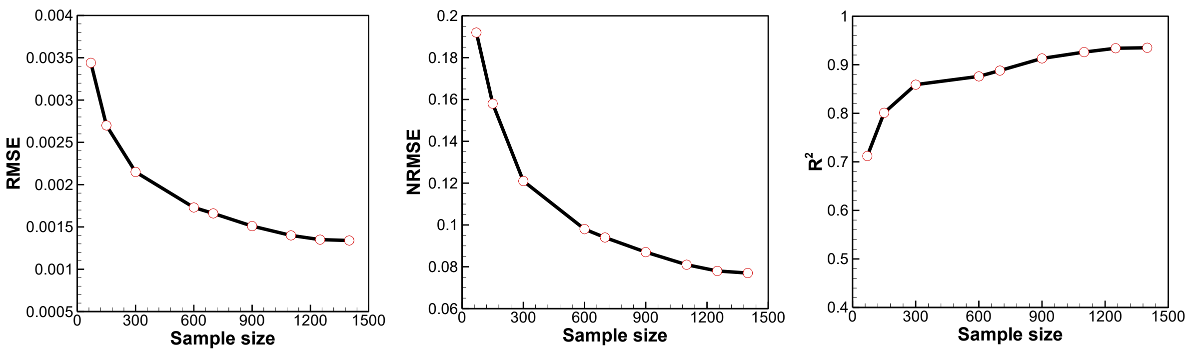


(a) (b) (c)

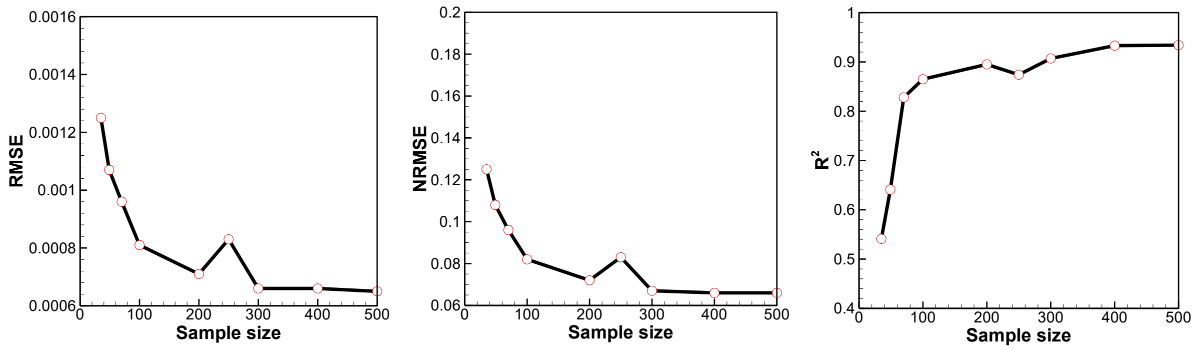


(d) (e) (f)

**Fig. 11.** Convergence of surrogate model performance metrics with increasing sample size. (a) low-fidelity RMSE; (b) low-fidelity NRMSE; (c) low-fidelity $R^2$; (d) high-fidelity RMSE; (e) high-fidelity NRMSE; (f) high-fidelity $R^2$.

Latin Hypercube Sampling (LHS) was used to generate representative heater-pad power-density inputs [W/m²] across the prescribed design space. Figures 12(a) and 12(b) show the resulting distributions for the low- and high-fidelity datasets, respectively. The low-fidelity sampling (Fig. 12(a)) consists of 1,250 data points. It exhibits dense, uniform coverage of the entire parameter space, reflecting the computational efficiency of the low-fidelity model and its suitability for broad initial exploration. In contrast, the high-fidelity dataset (Fig. 12(b)) contains approximately 400 samples, producing a sparser distribution due to the higher computational cost of these simulations. While less dense than the low-fidelity set, LHS ensures a uniform projection of these high-fidelity points onto each parameter axis, maintaining a good representation of the input variability despite the reduced sample count. This clear distinction in sample density between the low and high-fidelity datasets is fundamental to multi-fidelity optimization approaches, where inexpensive low-fidelity data are used for broad exploration, and selective high-fidelity data refine the understanding of complex relationships.

Figures 12(c) and 12(d) illustrate the pairwise relationships among the heater-pad power-density inputs for both fidelity levels. The off-diagonal scatter plots show no apparent linear or nonlinear trends, indicating the absence of artificial correlations and confirming that each heater-pad parameter is independently and uniformly distributed across the design space. This behavior is consistent in both the low- and high-fidelity datasets. The diagonal histograms further demonstrate that each parameter spans its entire prescribed range, exhibiting the expected uniform marginal distribution characteristic of Latin Hypercube Sampling. Collectively, these plots verify that the LHS strategy provides an efficient, unbiased, and well-stratified sampling foundation for developing reliable multi-fidelity models.

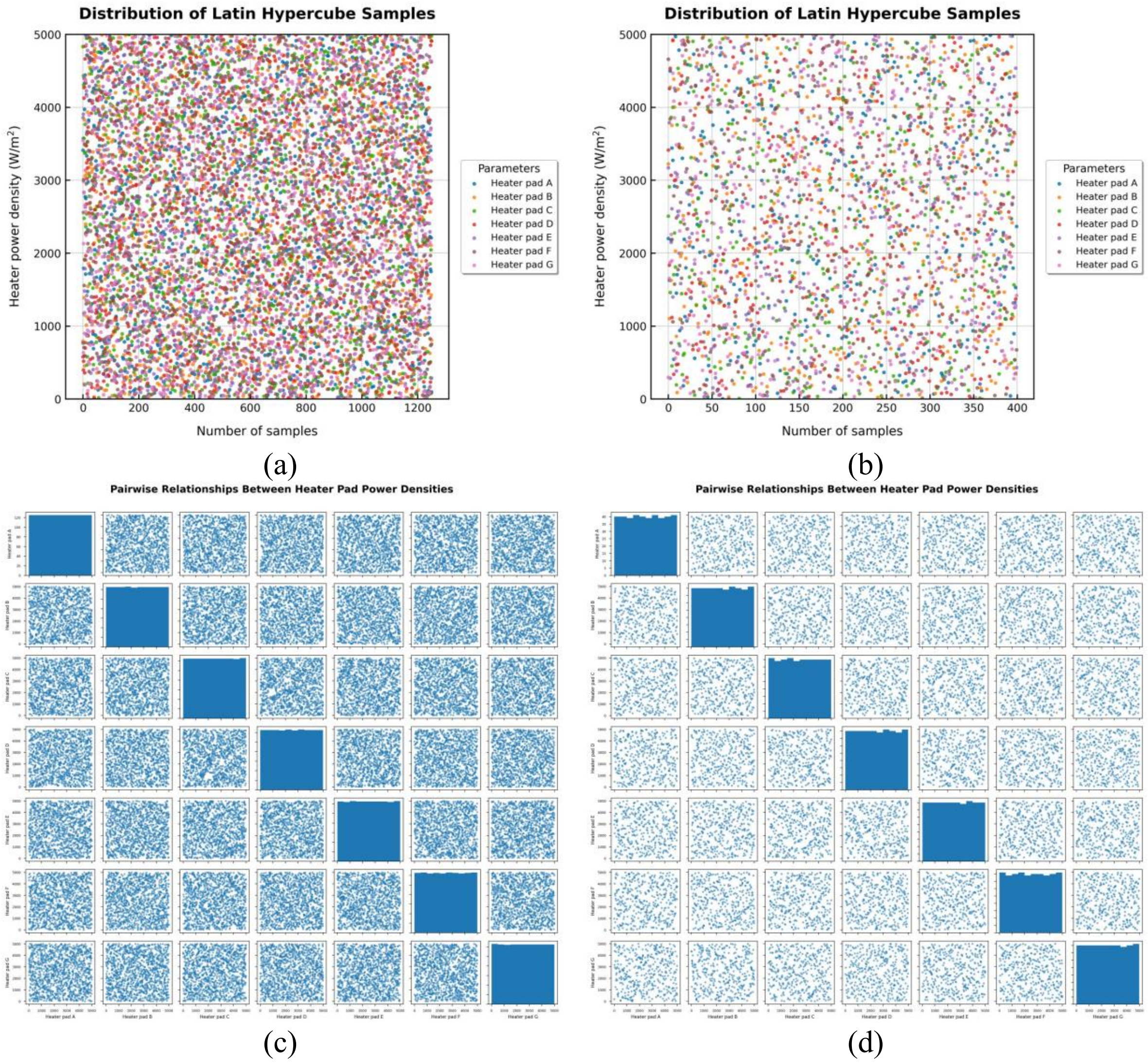


**Fig. 12.** Distributions and pairwise relationships of LHS used in the low-fidelity ((a), (c)) and high-fidelity ((b), (d)) simulations, illustrating the sampling coverage across the input space.

### 4.2. Surrogate model development and performance

This section presents a comprehensive analysis of the surrogate modeling strategy, encompassing the dimensionality reduction, performance evaluation, and refinement methodology. The results begin with dimensionality reduction using POD to compress high-dimensional simulation data while retaining essential features. The approach incorporates low-fidelity, high-fidelity, and multi-fidelity surrogate models, whose predictive capabilities are evaluated using $R^2$ and NRMSE metrics—demonstrating reliable prediction of critical constraints across both running-wet and evaporative regimes. To assess the impact of model fidelity on prediction accuracy, high-fidelity and low-fidelity simulations are compared with their corresponding surrogate models. This comparison highlights the importance of fidelity level in capturing key physical behaviors and its influence on model performance.

Notably, the multi-fidelity surrogate achieved accuracy comparable to high-fidelity simulations while significantly reducing computational cost and minimizing the need for extensive high-fidelity data. Additionally, the computational efficiency of this approach is quantified, further emphasizing its practicality.

To improve the model's performance even further, an error-driven iterative sampling strategy was employed, using leave-one-out cross-validation (LOOCV) and self-organizing maps (SOM) to guide targeted, efficient sampling.

#### 4.2.1. Dimensionality reduction via proper orthogonal decomposition

Figure 13 provides a detailed comparative analysis of temperature distributions along the protection limit, contrasting high-fidelity results from the high-fidelity simulations (solid black lines) with the corresponding predictions obtained using the POD model (dashed blue lines) across four representative test cases. All four cases share the same ice and flight conditions as case 22B in Table 3, but each subplot corresponds to a unique heater power density distribution. The specific heater power densities (in $W/m^2$) for heaters A through G used in these subplots are summarized in Table 5.

**Table 5**

Heater Power Densities (W/m²) for Subplots in Fig. 13.

| Heater | (a) Test case | (b) Training case | (c) Test case | (d) Training case |
|---|---|---|---|---|
| A | 669.31 | 449.88 | 3515.05 | 3665.80 |
| B | 297.21 | 789.03 | 3266.55 | 3829.96 |
| C | 733.78 | 348.35 | 4790.36 | 2859.78 |
| D | 421.69 | 972.77 | 3142.06 | 2271.65 |
| E | 492.05 | 422.53 | 3967.29 | 3362.92 |
| F | 547.18 | 465.24 | 3317.87 | 2032.83 |
| G | 952.12 | 166.61 | 3796.16 | 2476.20 |

Each subplot in Fig. 13 illustrates temperature values in Kelvin [K] as a function of the normalized spatial coordinate S/C along the protection limit. Subplots (a) and (b) correspond to cases in the running-wet regime and exhibit relatively uniform temperature profiles across the protected region, with a sharp temperature drop at the end of the protection limit—demonstrating the high-fidelity solver's ability to maintain consistent thermal performance. In contrast, subplots (c) and (d) represent cases in the evaporative regime, where more complex and non-uniform temperature distributions are observed due to varying heat transfer mechanisms. In all cases, the POD-based predictions show excellent agreement with the high-fidelity simulation results, confirming the accuracy and robustness of the POD model in capturing detailed thermal behaviors.

The output data used for constructing the surrogate model has an inherent dimensionality of 201 spatial points, resulting in a snapshot matrix of size 201 × 400, where 201 denotes spatial resolution, and 400 represents the number of high-fidelity simulations. Before applying the surrogate model, the POD method was employed to reduce the dimensionality of the spatial field from 201 to 80 POD modes, retaining 99.9% of the total energy. This reduction decreases the output dimension by approximately 60%, while preserving the essential physical information needed for accurate reconstruction. Regarding computational efficiency, the complete POD processing pipeline—including snapshot decomposition to create a data matrix, mode selection based on eigenvalue and eigenvector, POD coefficient computation, and field reconstruction—requires approximately 5 seconds for the entire set of snapshots. In contrast, a single high-fidelity simulation requires 1444 minutes to generate one snapshot. Therefore, the combined POD processing time is negligibly small compared to the original high-fidelity computational cost, confirming that POD-based dimensionality reduction significantly accelerates the overall workflow.

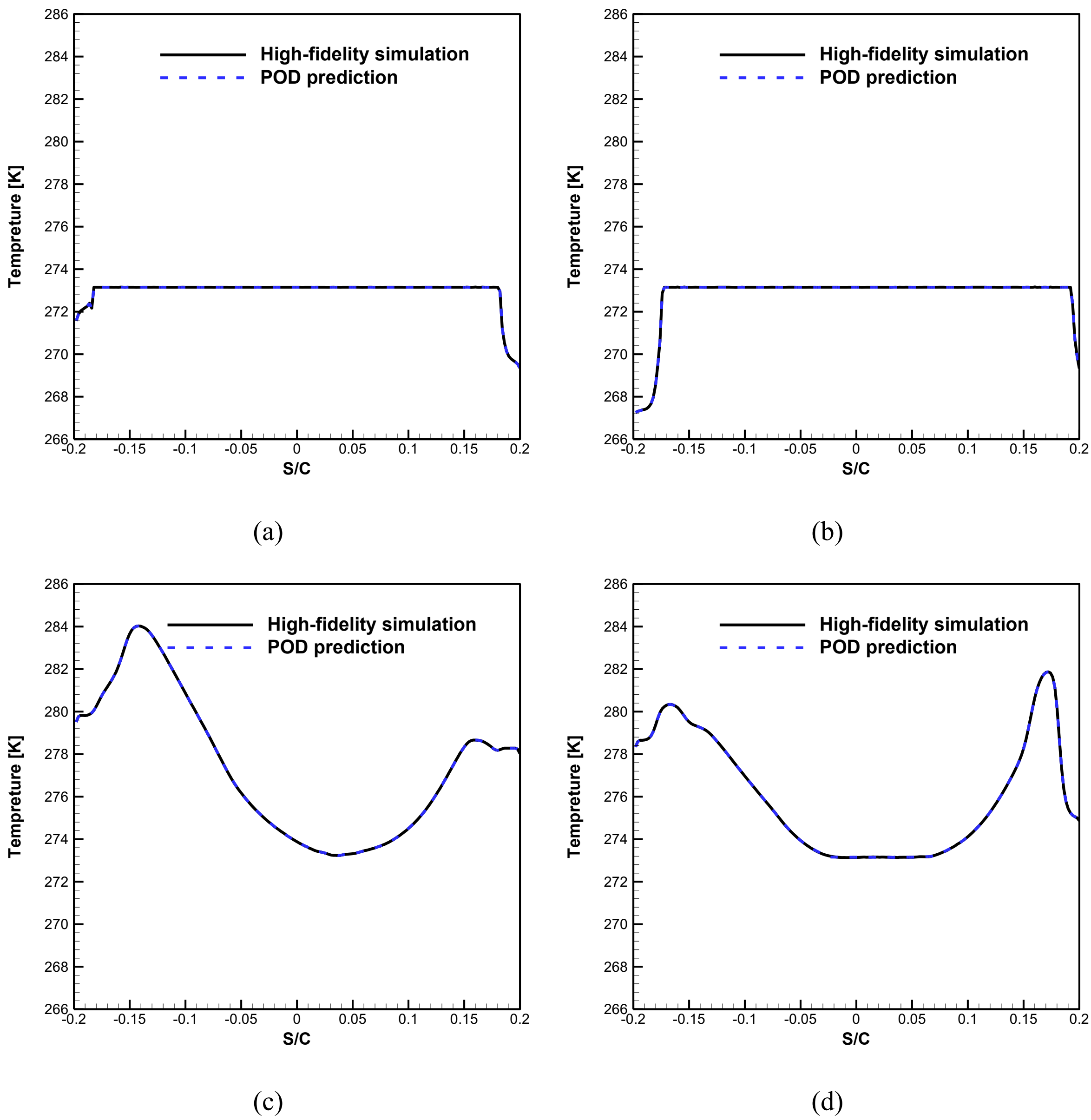


**Fig. 13.** Comparison of high-fidelity simulation and POD prediction for temperature distribution along the protection limit: (a), (b) running-wet regime; (c), (d) evaporative

regime.

#### 4.2.2. Surrogate model performance: single versus multi-fidelity approaches

Tables 6 and 7 present a detailed quantitative evaluation of the surrogate model accuracies across the multi-fidelity, low-fidelity, and high-fidelity approaches for both running-wet and evaporative anti-icing regimes. The datasets consist of 1,650 samples for the multi-fidelity model (1,080 for training and 570 for testing), 1,250 samples for the low-fidelity model (1,000 for training and 250 for testing), and 400 samples for the high-fidelity model (320 for training and 80 for testing).

Table 6, focusing on the running-wet regime, presents the NRMSE and $R^2$ metrics for the maximum ice growth and target wall temperature constraints. In this regime, the multi-fidelity model achieves strong predictive accuracy, with test $R^2$ values of 0.91 for maximum ice growth and 0.95 for target wall temperature, closely approaching the performance of the high-fidelity surrogate ($R^2$ of 0.95 for maximum ice growth and 0.98 for target wall temperature) while significantly reducing the number of high-fidelity simulations required.

Similarly, Table 7 evaluates the models for the evaporative regime, including an additional end film height constraint. Here, the multi-fidelity model maintains high accuracy, with Test $R^2$ values of 0.90 for maximum ice growth, 0.91 for end film height, and 0.90 for target wall temperature, again demonstrating competitive performance compared to the high-fidelity surrogate, which yields Test $R^2$ values of 0.91 for maximum ice growth, 0.96 for end film height, and 0.93 for target wall temperature. Across both regimes and all constraints, the multi-fidelity surrogate consistently provides a favorable balance between accuracy and computational efficiency, demonstrating its ability to approximate high-fidelity outputs effectively while leveraging the computational benefits of lower-fidelity data.

**Table 6**

Accuracy comparison of multi-fidelity, low-fidelity, and high-fidelity surrogate models for maximum ice growth (MIG) and target wall temperature (TWT) constraints for running-wet regime using normalized RMSE and $R^2$ metrics.

| Constraint | Multi-Fidelity | | | | Low-Fidelity | | | | High-Fidelity | | | |
|---|---|---|---|---|---|---|---|---|---|---|---|---|
| | NRMSE | | $R^2$ | | NRMSE | | $R^2$ | | NRMSE | | $R^2$ | |
| | Test | Train | Test | Train | Test | Train | Test | Train | Test | Train | Test | Train |
| MIG | **0.07** | **0.05** | **0.91** | **0.94** | **0.03** | **0.02** | **0.98** | **0.99** | **0.06** | **0.04** | **0.95** | **0.96** |
| TWT | **0.06** | **0.03** | **0.95** | **0.98** | **0.04** | **0.03** | **0.97** | **0.99** | **0.05** | **0.04** | **0.98** | **0.99** |

**Table 7**

Accuracy comparison of multi-fidelity, low-fidelity, and high-fidelity surrogate models for maximum ice growth (MIG), end film height (EFH), and target wall temperature (TWT) constraints for evaporative regime using normalized RMSE and $R^2$ metrics.

| Constraint | Multi-Fidelity | | | | Low-Fidelity | | | | High-Fidelity | | | |
|---|---|---|---|---|---|---|---|---|---|---|---|---|
| | NRMSE | | $R^2$ | | NRMSE | | $R^2$ | | NRMSE | | $R^2$ | |
| | Test | Train | Test | Train | Test | Train | Test | Train | Test | Train | Test | Train |
| MIG | **0.09** | **0.07** | **0.9** | **0.93** | **0.05** | **0.03** | **0.92** | **0.96** | **0.07** | **0.05** | **0.91** | **0.95** |
| EFH | **0.08** | **0.05** | **0.91** | **0.98** | **0.08** | **0.06** | **0.94** | **0.97** | **0.06** | **0.05** | **0.96** | **0.99** |
| TWT | **0.07** | **0.05** | **0.9** | **0.97** | **0.03** | **0.02** | **0.97** | **0.99** | **0.06** | **0.04** | **0.93** | **0.98** |

### A. Comparison of low-fidelity simulations and surrogate model predictions

Figure 14 provides a comparative analysis of the surrogate model's performance in predicting temperature distributions along the protection limit against low-fidelity simulations. The figure comprises four subplots, each displaying temperature in Kelvin [K] as a function of the normalized chord position (S/C). All of the subplots share the same ice and flight conditions as case 22B in Table 3, but each corresponds to a unique heater power density distribution. Specifically, subplots (a) and (c) present results for test cases, while subplots (b) and (d) illustrate training cases. The precise heater power densities (in W/m²) for heaters A through G used in these subplots are summarized in Table 8.

**Table 8**

Heater power densities (W/m²) for subplots in Fig. 14.

| Heater | (a) Test case | (b) Training case | (c) Test case | (d) Training case |
|---|---|---|---|---|
| A | 1435.16 | 4300.2 | 4843.63 | 1136.22 |
| B | 2807.11 | 4617.78 | 2431.69 | 4987.78 |
| C | 3964.63 | 3184.73 | 4032.57 | 3919.45 |
| D | 4470.65 | 4856.63 | 2466.01 | 2000.93 |
| E | 3626.27 | 4529.98 | 4679.87 | 3848.49 |
| F | 1335.97 | 260.47 | 1215.35 | 3981.85 |
| G | 2800.48 | 152.04 | 2574.45 | 4844.16 |

In each subplot in Fig. 14, the low-fidelity simulation results are shown as solid black lines with white circular markers, while the low-fidelity surrogate model predictions are displayed as red lines with blue circular markers. In all cases, the temperature distribution shows sharp changes in trend. This behavior occurs because the heat source is applied directly to the surface along the protection limit, which leads to sudden variations in temperature at the locations of each heater pad. These sharp transitions are expected due to the localized nature of the heating. The comparison shows very good agreement between the surrogate model and the low-fidelity simulation in both the test cases (subplots a and c) and training cases (subplots b and d), confirming that the surrogate model can accurately reproduce the thermal behavior captured by the original simulations.

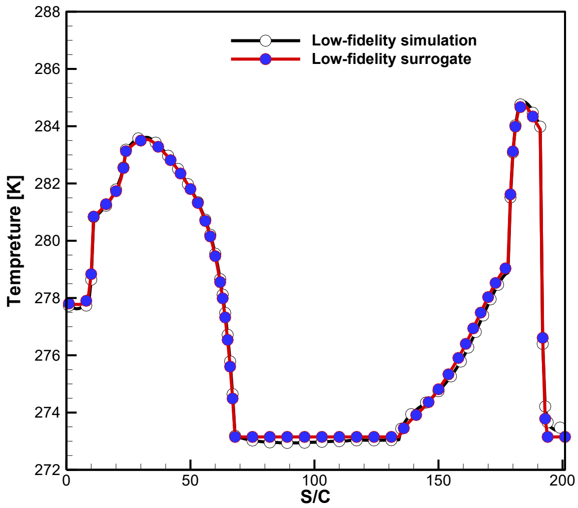


(a)

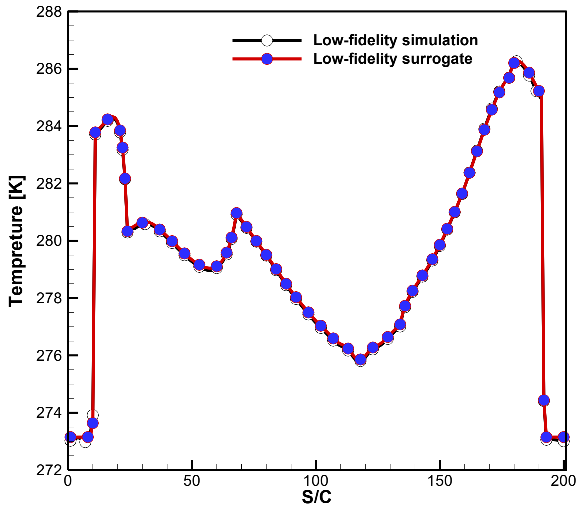


(b)

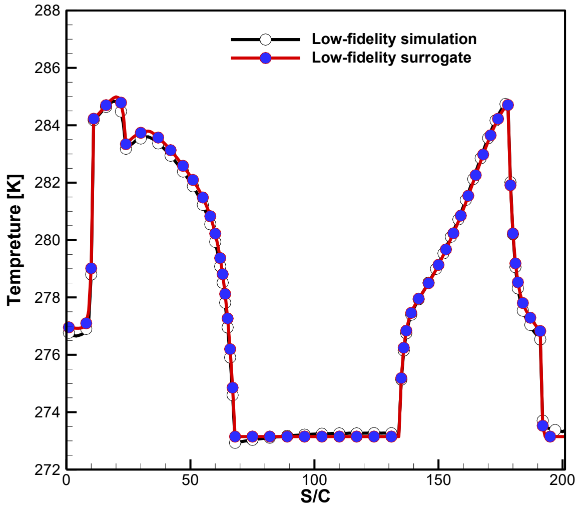


(c)

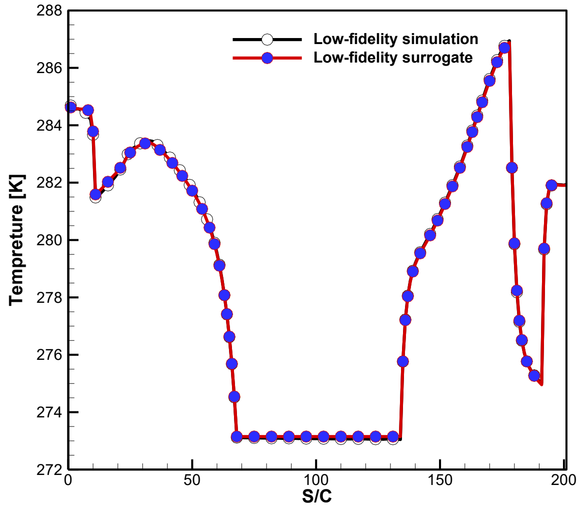


(d)

**Fig. 14.** Temperature distribution along the protection limit: (a, c) test cases comparing low-fidelity surrogate vs. low-fidelity simulation; (b, d) train cases comparing low-fidelity surrogate vs. low-fidelity simulation.

### B. Comparison of high-fidelity simulations and surrogate model predictions

Figure 15 provides a comparative analysis of the surrogate model's performance in predicting temperature distributions along the protection limit against high-fidelity simulations from the IPS. The figure comprises four subplots, each displaying temperature in Kelvin [K] as a function of the normalized chord position (S/C). All of the subplots share the same ice and flight conditions as case 22B in Table 3, but each corresponds to a unique heater power density distribution. Specifically, subplots (a) and (c) present results for test cases, while subplots (b) and (d) illustrate training cases. The precise heater power densities (in W/m²) for heaters A through G used in these subplots are summarized in Table 9.

**Table 9**

Heater Power Densities (W/m²) for Subplots in Fig. 15.

| Heater | (a) Test case | (b) Training case | (c) Test case | (d) Training case |
|---|---|---|---|---|
| A | 578.72 | 960.65 | 2200.41 | 4577.31 |
| B | 559.37 | 500.94 | 2111.29 | 2875.88 |
| C | 587.48 | 533.86 | 2737.64 | 4132.81 |
| D | 326.17 | 536.80 | 3508.10 | 4977.80 |
| E | 950.74 | 698.99 | 2121.64 | 4559.44 |
| F | 181.83 | 598.19 | 2383.96 | 2646.33 |
| G | 606.49 | 138.70 | 4039.39 | 2747.56 |

In each subplot in Fig. 15, the high-fidelity simulation results are shown as solid black lines with circular white markers, while the high-fidelity surrogate model predictions are represented by red lines with circular blue markers. The top row (subplots a and b) shows cases with relatively uniform heating patterns, where the high-fidelity surrogate model accurately captures the consistent thermal response. In contrast, the bottom row (subplots c and d) presents more complex temperature distributions, typically caused by intricate heat transfer mechanisms.

It is important to note that, unlike the low-fidelity simulations—which showed sharp temperature changes at each heater pad—the high-fidelity results display smoother temperature variations. This is because a conduction solver was used in the high-fidelity model. Across all test cases (a, c) and training cases (b, d), the high-fidelity surrogate model demonstrates strong agreement with the high-fidelity simulations, effectively capturing both overall trends and localized variations.

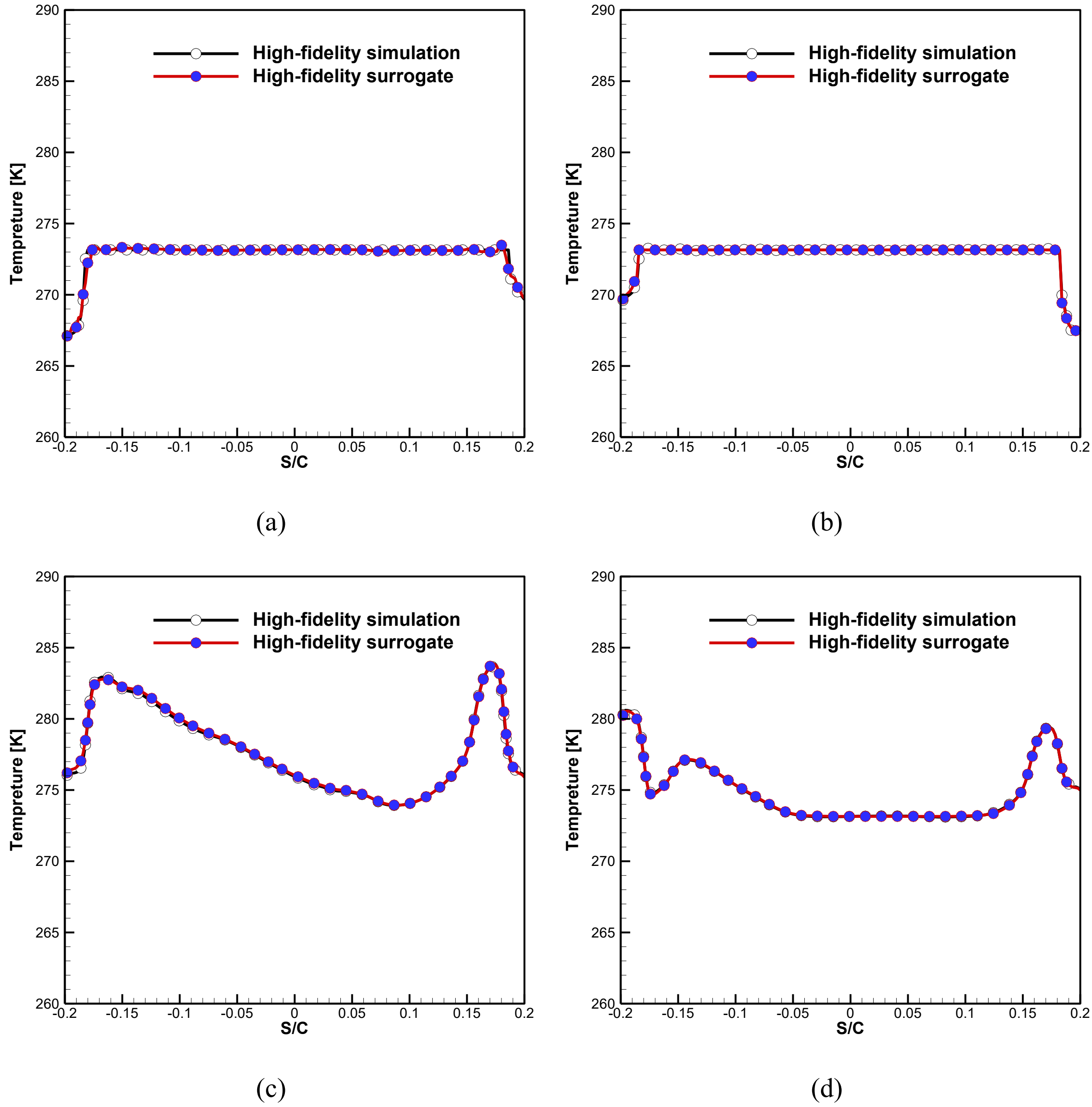


**Fig. 15.** Temperature distribution along the protection limit: (a, c) test cases comparing high-fidelity surrogate vs. high-fidelity simulation; (b, d) train cases comparing high-fidelity surrogate vs. high-fidelity simulation.

### C. Comparison of high-fidelity simulations and multi-fidelity surrogate model predictions

Figure 16 provides a comprehensive comparison of the multi-fidelity surrogate model (MFSM)'s predictive accuracy for temperature distributions under running wet conditions. It comprises four subplots, each illustrating temperature (in Kelvin) as a function of the normalized position along the protection limit (S/C). All of the subplots share the same ice and flight conditions as case 22B in Table 3, but each corresponds to a unique heater power density distribution. Specifically, subplots (a) and (c) present results for test cases, while subplots (b) and (d) illustrate training cases. The precise heater power densities (in $W/m^2$) for heaters A through G used in these subplots are summarized in Table 10.

**Table 10**

Heater Power Densities ($W/m^2$) for Subplots in Fig. 16.

| Heater | (a) Test case | (b) Training case | (c) Test case | (d) Training case |
|---|---|---|---|---|
| A | 774.11 | 182.81 | 4577.31 | 3575.21 |
| B | 669.27 | 422.86 | 2875.88 | 4836.13 |
| C | 249.79 | 760.49 | 4132.81 | 4433.49 |
| D | 234.74 | 394.40 | 4977.80 | 399.76 |
| E | 875.69 | 241.11 | 4559.44 | 3908.61 |
| F | 330.35 | 453.73 | 2646.33 | 2558.65 |
| G | 34.08 | 198.94 | 2747.56 | 636.23 |

In these subplots in Fig. 16, high-fidelity simulation results are represented by solid black lines with circular white markers, while predictions from the MFSM are shown as red lines with circular blue markers. The top row displays test cases (subplots a and b) characterized by relatively uniform temperature profiles across the protected surface, indicating consistent thermal performance. In contrast, the bottom row captures cases (subplots c and d) with spatially varying temperature distributions, reflective of the non-uniform heat transfer. Across all cases, the MFSM demonstrates strong concordance with the high-fidelity results, accurately replicating both global temperature trends and localized variations. This level of agreement highlights the surrogate model's robustness in modeling complex thermal behaviors relevant to anti-icing applications.

Importantly, the adoption of a multi-fidelity framework enabled a 75% reduction in high-fidelity simulation requirements (from 400 to 100), yielding substantial computational savings without significant loss in predictive accuracy. While the performance is marginally less precise than the results in Fig. 12—which were based exclusively on high-fidelity data—the model trained using the combination of low-fidelity and a limited set of high-fidelity data effectively approximated high-fidelity outputs with significantly reduced training demands.

Additionally, the GPR and MFGPR models, when combined with POD, achieved over 95% accuracy in predicting temperature fields under stratiform cloud icing and continuous maximum icing envelope conditions. This MFGPR-POD and GPR-POD surrogate modeling approach also significantly reduced computational cost, cutting simulation time by 99.998%—from 1444 minutes to just 0.03 minutes—demonstrating both high efficiency and accuracy for thermal analysis in IPS applications. Due to the tightly coupled conjugate heat-transfer (CHT) framework with sub-iterations between the ice and conduction solvers, the high-fidelity simulations incur a high computational cost.

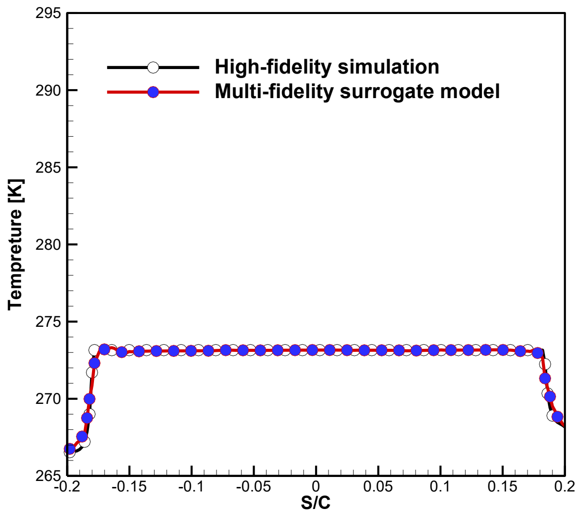

(a)

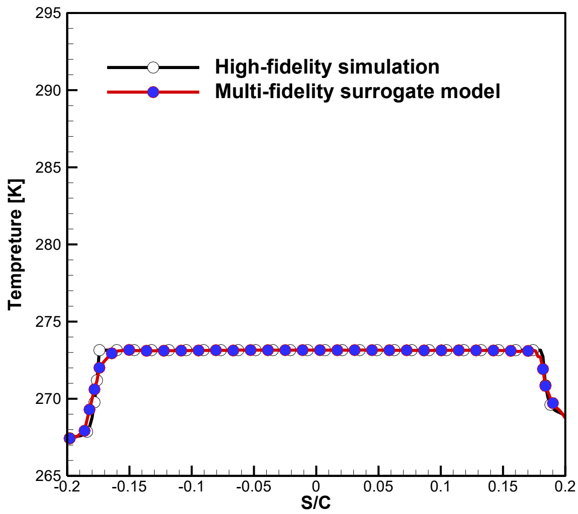

(b)

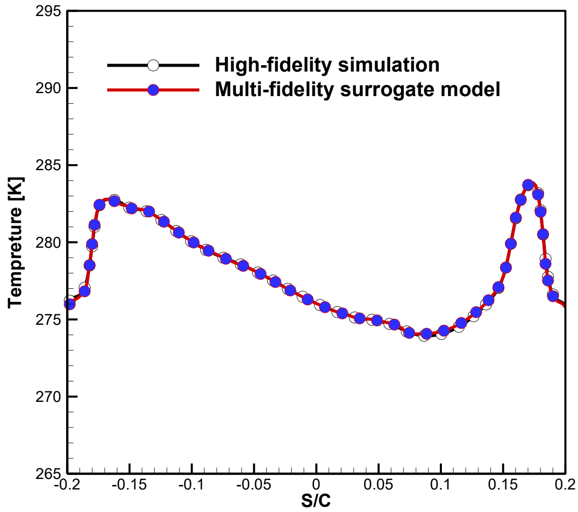


(c)

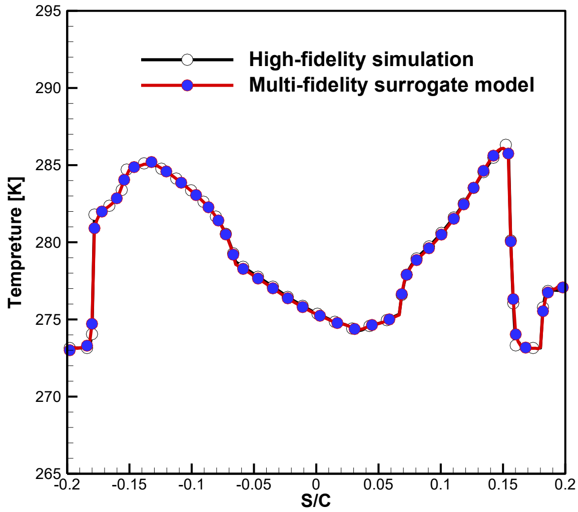


(d)

**Fig. 16.** Temperature distribution along the protection limit: (a, c) test cases comparing MFSM vs. high-fidelity simulation; (b, d) train cases comparing MFSM vs. high-fidelity simulation.

#### 4.2.3. Model refinement via error-driven iterative sampling

A clustering analysis of the error-driven iterative sampling methodology was systematically executed utilizing the SOM algorithm, a sophisticated unsupervised neural network approach that provides topologically preserved dimensionality reduction and pattern recognition capabilities for high-dimensional data spaces. The identification and selection of newly updated sample points were methodically determined through the implementation of k-means clustering algorithms applied to the trained SOM network, which enables efficient exploration of the design space while maintaining computational tractability and ensuring representative coverage of critical regions exhibiting elevated prediction uncertainties. Figure 17 comprehensively illustrates the spatial distribution and evolution of sampling points, presenting both the initial sample configuration and the final optimized sample distribution achieved through the iterative refinement process.

By systematically applying SOM-based analysis and subsequent adaptive sampling strategies, a total of 400 high-fidelity simulation snapshots were strategically acquired and incorporated into the training dataset, representing a substantial enhancement in the representational capacity of the surrogate modeling framework. The comparative assessment of maximum temperature prediction errors between the initial and final stages, as depicted in Fig. 17, demonstrated a significant improvement in predictive accuracy. The maximum error magnitude exhibited an approximate 25 percent reduction following the strategic incorporation of additional sample points in critical regions characterized by high error gradients and complex thermal behavior. This substantial error reduction not only validates the efficacy of the error-driven adaptive sampling approach but also confirms the enhanced accuracy and reliability of each surrogate model within the multi-fidelity modeling framework, thereby establishing a more robust and precise computational tool for thermal analysis of composite structures under various operating conditions.

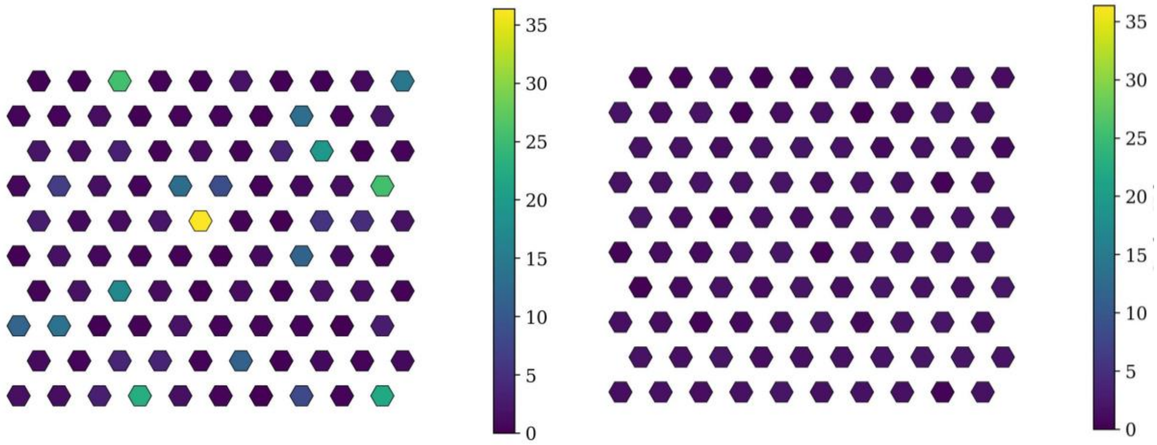


**Fig. 17.** Initial (left) and final (right) SOM analysis on the anti-ice surface using the average LOOCV error.

### 4.3. Multi-fidelity surrogate optimization (MFSO) results

#### 4.3.1. Running-wet regime optimization

This section presents the results of the multi-fidelity surrogate-based optimization applied to the running-wet anti-icing regime. The optimization problem was formulated with two distinct constraints: target wall temperature and maximum ice growth, both sharing a common objective function, which is the minimization of total electric power.

**A. Target wall temperature constraint**

This subsection details the formulation of the target wall temperature constraint, which serves as a critical component in the multi-fidelity surrogate optimization problem. The objective here is to minimize the deviation of the predicted wall temperature T(s) from a desired target temperature profile $T_0(s)$ along the protection limit. By minimizing this integral, the optimization seeks to achieve a uniform and desired temperature distribution across the heated zone, while simultaneously considering the overall objective of minimizing total electric power.

Figure 18 presents the convergence behavior of the multi-fidelity surrogate-based optimization process for achieving the target wall temperature in the running wet anti-icing regime. The figure comprises three subplots, each illustrating the evolution of key optimization metrics with respect to the number of evaluations.

Subplot (a) shows the convergence of individual heater power densities [$W/m^2$] for Heaters A to G. Although the initial power allocations varied widely, all values gradually converge to stable, optimized levels after approximately 400 evaluations, suggesting that a minimum of 400 iterations is required to achieve reliable power distribution across the heating elements. Subplot (b) illustrates the convergence of the target wall temperature in $T_0$ = 276 K, the objective function. A rapid reduction in deviation from the desired temperature was observed during early evaluations, followed by stabilization at a minimal error below 0.1 K—demonstrating the optimization's effectiveness in aligning actual and target wall temperatures. Subplot (c) depicts the convergence of the total electric power [W], which stabilizes around 550 W.

Overall, these plots collectively validate the robustness and efficiency of the multi-fidelity surrogate optimization framework for determining optimal operational parameters to maintain the target wall temperature in the running wet anti-icing mode.

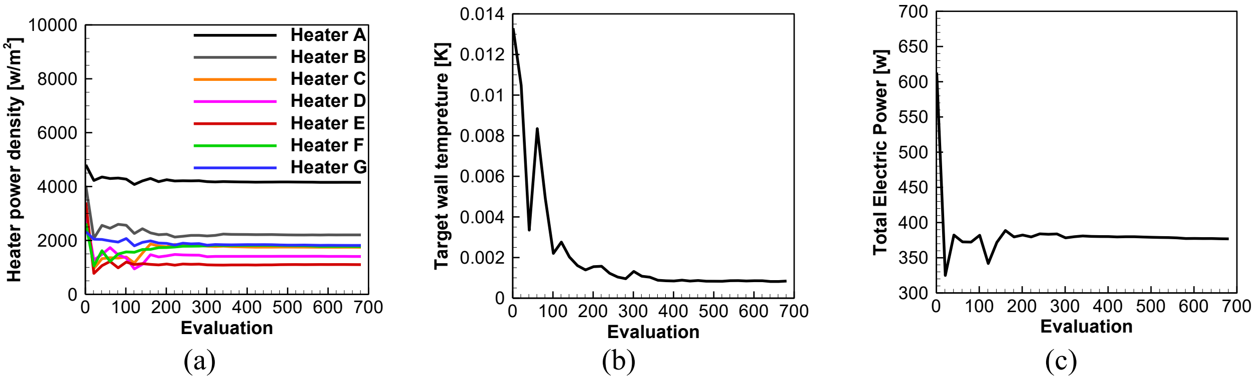


**Fig. 18.** Convergence history of MFSO for target wall temperature constraint in $T_0$ = 274 K: (a) Heater power density evolution, (b) target wall temperature convergence, (c) total electric power consumption.

Figure 19 presents a comprehensive performance comparison and analysis of MFSO versus baseline anti-icing configurations, demonstrating the effectiveness of the proposed optimization framework through four key analytical perspectives. Subplot (a) illustrates the spatial power density requirements across the normalized chord position for varying target wall temperatures, revealing how power distribution adapts to different thermal objectives while maintaining efficient energy allocation along the protection surface. Subplot (b) demonstrates the relationship between total electric power and target wall temperature across various $T_0$ values (273.2 K, 274 K, 275 K, 276 K, 278 K, and 280 K), showing a clear increase in power requirements as temperature targets rise. Subplot (c) provides a direct overall power efficiency comparison between the optimized and baseline configurations, highlighting the significant reduction in total power consumption achieved through the MFSO approach, with the optimized system requiring substantially lower power density to maintain equivalent thermal protection performance. Finally, subplot (d) presents individual heater power density analysis across all heating pads (A to G), showing how the optimization redistributes power allocation among individual heaters to achieve more efficient thermal management compared to the baseline approach.

Collectively, these results show the superior performance of the MFSO methodology, achieving a 38.5% improvement in power efficiency while maintaining robust anti-icing capabilities, thereby demonstrating the practical value of advanced optimization techniques in thermal management system design.

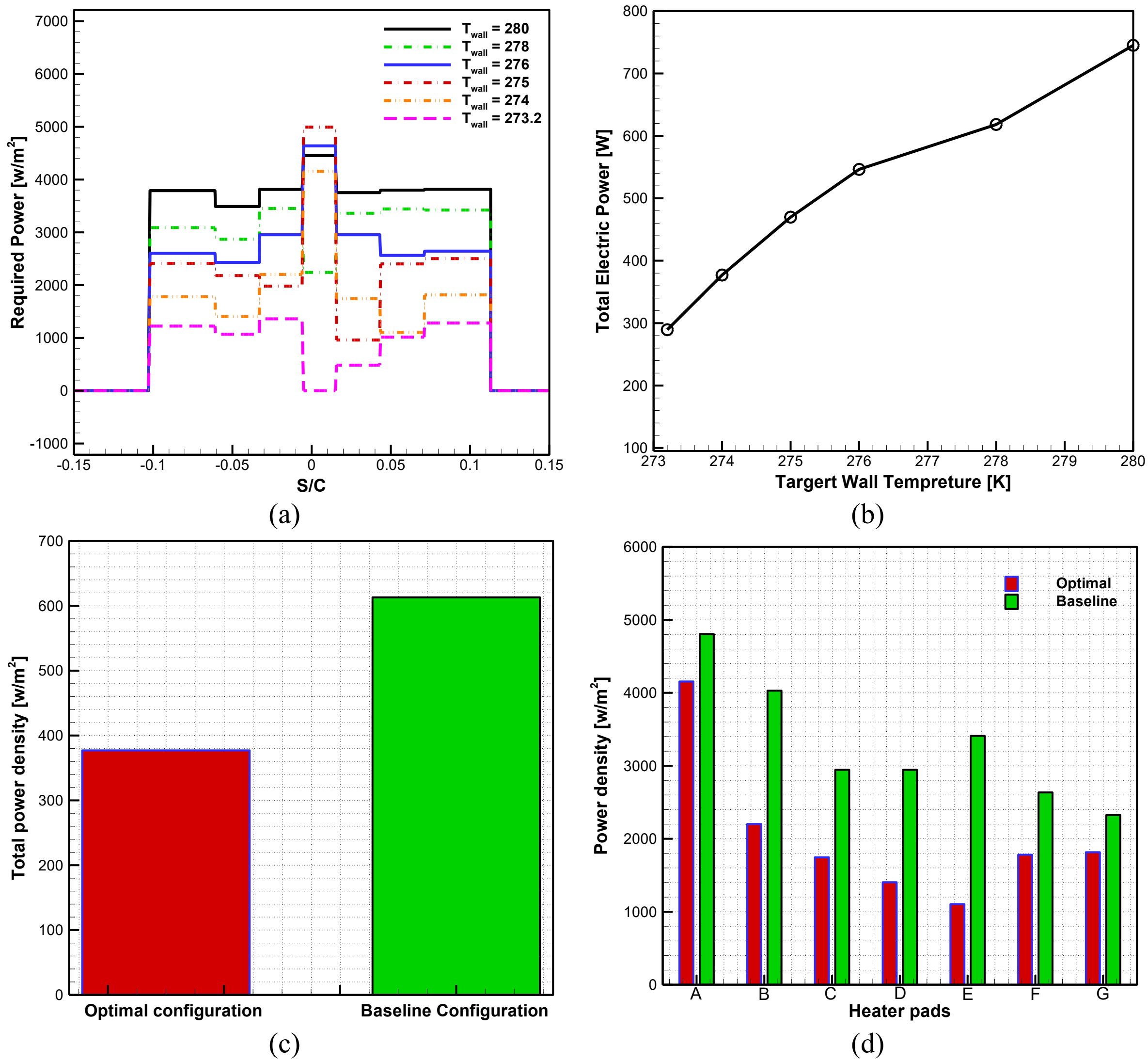


**Fig. 19.** Performance comparison and analysis of MFSO versus baseline anti-icing configurations: (a) Spatial power density requirements for varying target wall temperatures, (b) total electric power consumption versus target wall temperature, (c) Overall power efficiency comparison, (d) Individual heater power density analysis in $T_0$ = 274 K.

Figure 20 compares the ice shape, water film, and temperature contours for (a) the baseline configuration and (b) the optimal configuration (case 22B) under the constraint target wall temperature at $T_0$ = 274 K. The color contour represents the surface temperature distribution, ranging from 266 K to 282 K, while the black and blue regions correspond to ice and water formation, respectively. In the baseline case, the runback ice beyond the protection limit is considerably larger than in the optimal configuration. Such a difference in ice shape can induce flow separation, leading to aerodynamic degradation characterized by increased drag and reduced lift. This clearly highlights the significance of the optimization process, where, with approximately 38% lower total electric power, a substantially improved runback ice shape is achieved.

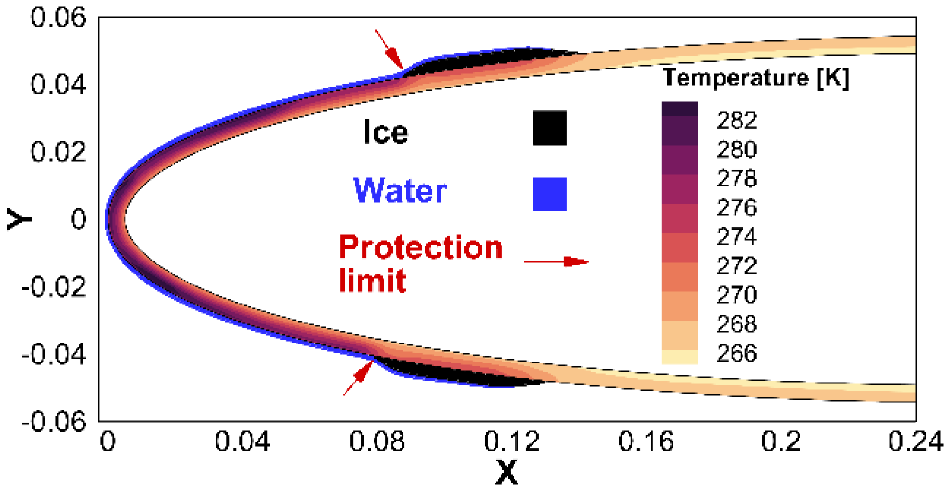


(a)

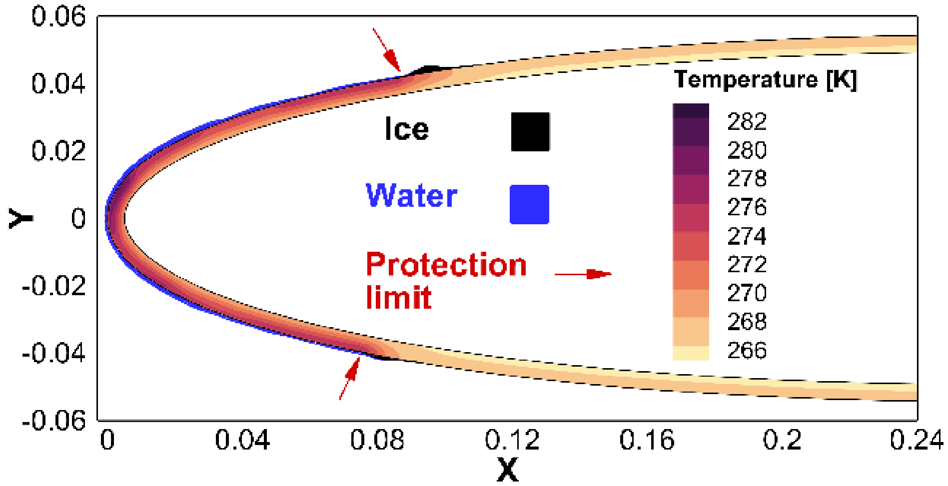


(b)

**Fig. 20.** Comparison of ice shape, water film, and temperature contours of (a) Baseline configuration and (b) Optimal configuration (case 22B) for constraint target wall temperature in $T_0 = 274$ K.

## B. Maximum ice growth constraint

In maximum ice growth, the primary objective is to maintain ice-free surfaces within the protection limits while minimizing total electric power for an energy-efficient anti-icing solution in running wet conditions. Figure 21 shows the convergence behavior of the MFSO under the maximum ice growth constraint through three plots. Subplot (a) illustrates the convergence of heater power densities [W/m²] for Heaters A–G, which stabilize around optimal values after initial fluctuations, indicating balanced power allocation. Subplot (b) depicts the convergence of the maximum ice growth constraint, with ice mass flux rapidly decreasing from ~4E-05 to near zero within 150 evaluations, confirming the effective minimization of ice accretion. Subplot (c) shows total electric power [W] stabilizing at 445 W after 400 evaluations, demonstrating that the surrogate model identifies energy-efficient solutions while satisfying anti-icing requirements. These results confirm the MFSO's capability to manage both energy consumption and ice accretion constraints effectively.

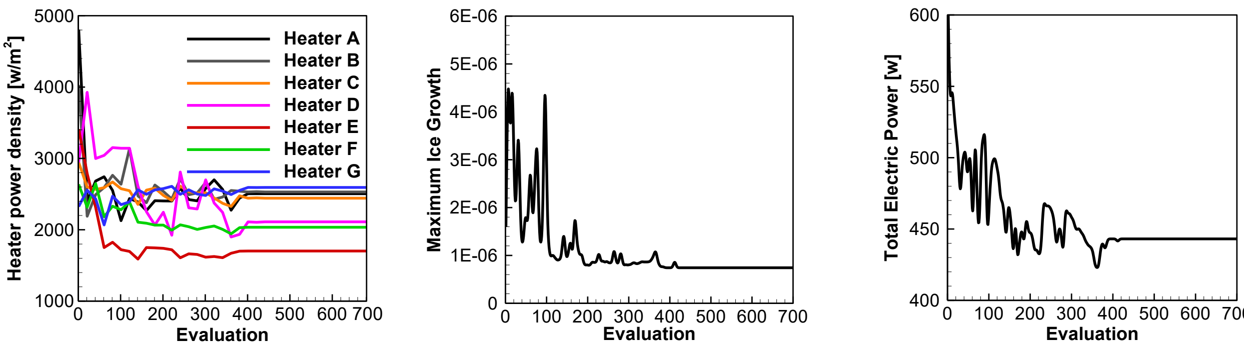

(a) (b) (c)

**Fig. 21.** Convergence history of MFSO for maximum ice growth constraint: (a) Heater power density evolution, (b) maximum ice growth convergence, (c) total electric power consumption.

Figure 22 compares optimized and baseline anti-icing configurations under the maximum ice growth constraint. Subplot (a) highlights a reduction in total electric power from 620 W/m² (baseline) to 445 W/m² (optimized), representing a 28% improvement in power efficiency. Subplot (b) shows power distribution across heaters A–G, where the optimized configuration strategically redistributes and reduces heater loads while maintaining effective thermal protection. This intelligent allocation ensures significant energy savings and strict adherence to the maximum ice growth constraint.

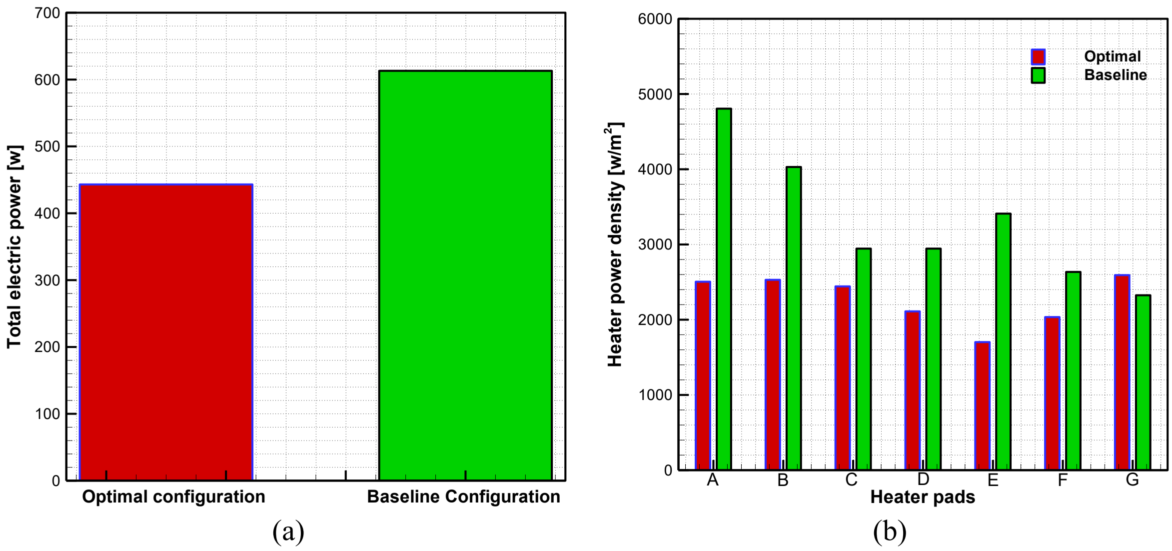


**Fig. 22.** Performance comparison of MFSO versus baseline configuration under maximum ice growth constraint: (a) Total electric power density comparison, (b) Individual heater power density distribution.

Figure 23 compares the ice shape, water film, and surface temperature distribution for (a) the baseline configuration and (b) the optimal configuration (case 22B) under the maximum ice growth constraint. The temperature field ranges from 266 K to 282 K, with black regions denoting ice accretion and the blue regions indicating the water film. In the baseline case, the extensive runback ice beyond the protection limit promotes flow separation, resulting in aerodynamic penalties due to increased drag and reduced lift. In contrast, the optimal configuration substantially reduces runback ice, demonstrating the effectiveness of the optimization at improving aerodynamic performance while lowering the total electric power demand by approximately 28%. However, this reduction in ice shape was higher for the target wall temperature constraint than here.

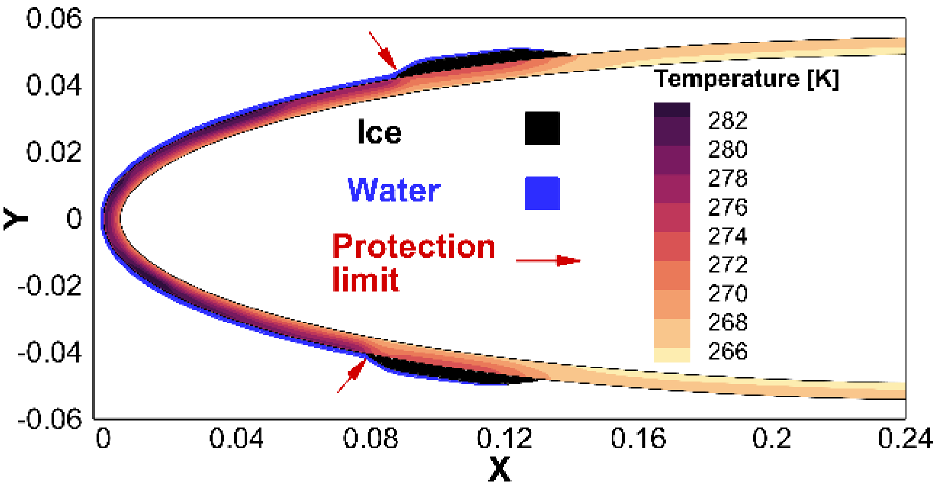


(a)

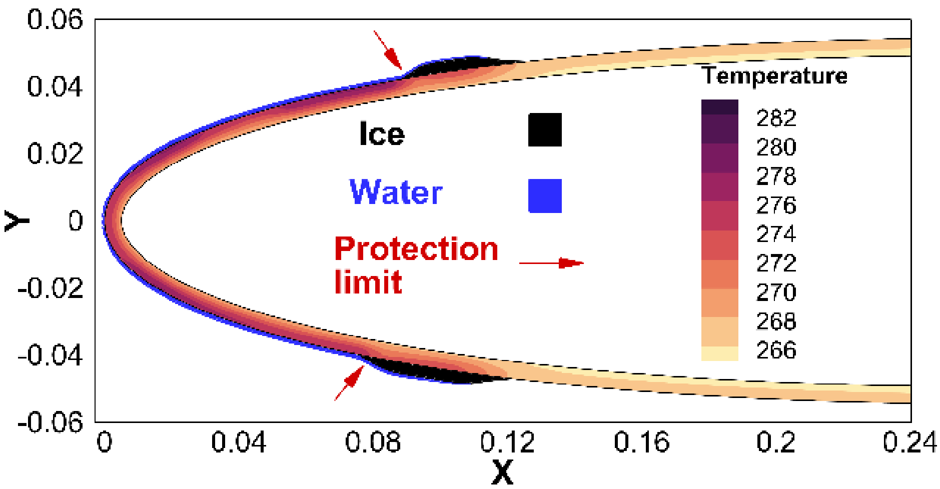


(b)

**Fig. 23.** Comparison of ice shape, water film, and temperature contours of (a) Baseline configuration and (b) Optimal configuration (case 22B) for constraint maximum ice growth.

### 4.3.2. Multi-fidelity surrogate optimization results for evaporative regime

In the evaporative anti-icing regime, the optimization problem was formulated with two main constraints: end film height and maximum ice growth. Figure 24 shows the convergence of the MFSO approach, confirming its effectiveness at balancing thermal management and icing constraints. Subplot (a) demonstrates the optimizer’s ability to minimize end film height, promoting efficient water evaporation and reducing downstream icing risk. Subplot (b) shows the successful reduction and stabilization of the maximum ice growth constraint, validating the reliability of the proposed strategy. Subplot (c) depicts the convergence of heater power densities [W/m²] across all heating elements (A–G), while subplot (d) illustrates the stabilization of total electric power [W], collectively demonstrating the framework's capacity to achieve energy-efficient anti-icing performance.

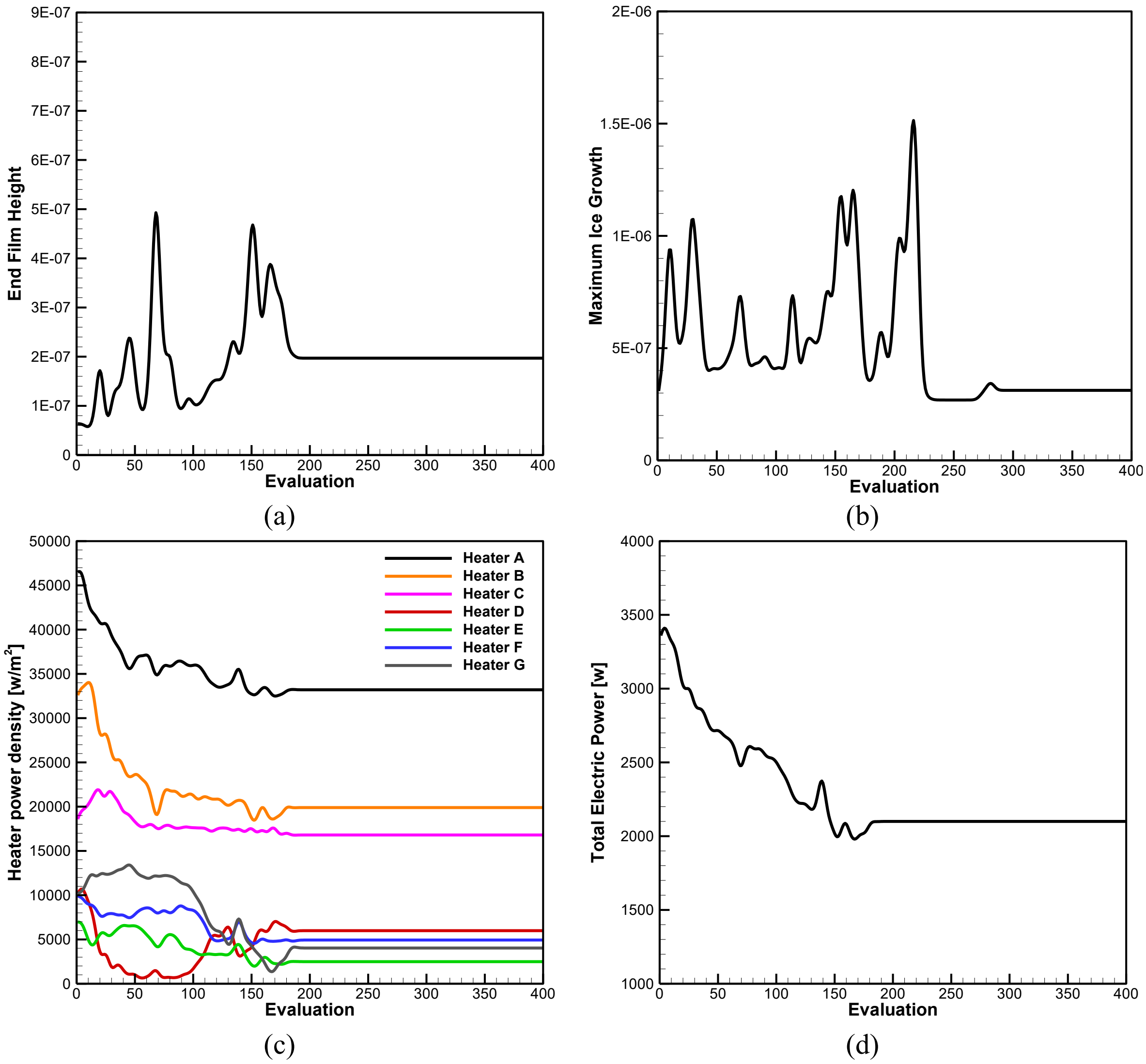


**Fig. 24.** Convergence history of MFSO in the evaporative anti-icing regime: (a) end film height evolution, (b) maximum ice growth constraint satisfaction, (c) Individual heater power density optimization, (d) total electric power minimization.

Figure 25 provides a detailed performance evaluation comparing the power utilization characteristics of the optimized and baseline anti-icing systems, illustrating the exceptional effectiveness and tangible advantages of the MFSO methodology in challenging thermal control applications. Subplot (a) illustrates the total electric power density [W/m²] requirements for both the optimal and baseline configurations, clearly demonstrating that the optimized configuration achieves a substantial reduction in total power density compared to the baseline system, with the optimal solution requiring approximately 2,000 W/m² compared to the baseline's 3,300 W/m². This represents a remarkable 40% improvement in overall power efficiency and energy utilization. This significant reduction in power consumption validates the effectiveness of the advanced optimization methodology in identifying highly efficient thermal management solutions while maintaining robust anti-icing performance under evaporative conditions.

Subplot (b) provides a detailed granular analysis of the power density [W/m²] distribution supplied to each heater pad (A through G) for both the optimal and baseline configurations, revealing the sophisticated optimization strategy employed by the algorithm. This comprehensive breakdown demonstrates that the optimization framework strategically redistributes thermal loads and, in most instances, significantly reduces the power input requirements for individual heating elements, with particularly notable reductions observed in heater pads A, B, and C, while maintaining adequate thermal protection across the entire heated zone. This intelligent and adaptive power management approach contributes directly to the substantial overall energy savings while ensuring effective anti-icing performance and complete water evaporation under challenging evaporative operating conditions.

These results comprehensively confirm the substantial practical benefits and superior performance of the MFSO framework, delivering significant energy efficiency improvements in anti-icing systems while fully preserving ice prevention capabilities and thermal protection effectiveness through substantial computational cost reduction achieved by strategically combining high-fidelity simulations with computationally efficient low-fidelity simulations. While this study focuses on the NACA0012 airfoil, the proposed multi-fidelity surrogate optimization framework is not limited to a specific airfoil geometry. With appropriate retraining, it can be applied to other airfoils, but specific performance may vary.

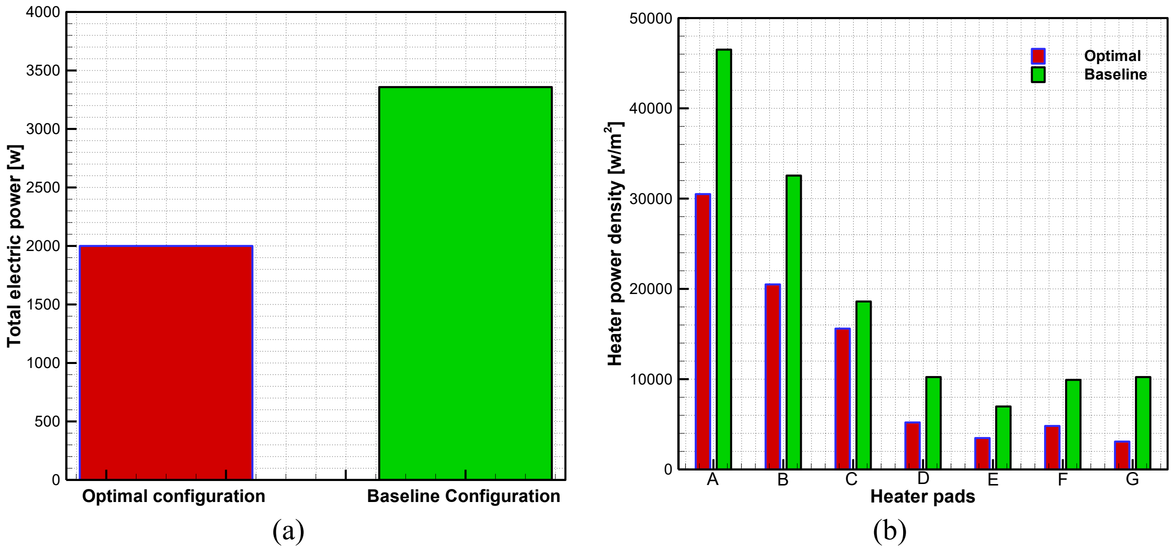


**Fig. 25.** Comparative analysis of power consumption for optimal versus baseline anti-icing configurations in evaporative regime: (a) total electric power density comparison, (b) Individual heater power density distribution.

## 5. Conclusion and future work

This study developed a multi-fidelity surrogate-based optimization framework for electrothermal anti-icing systems. The novel multi-fidelity surrogate model integrates low- and high-fidelity simulations to reduce reliance on computationally expensive high-fidelity evaluations while retaining high predictive accuracy. High-fidelity simulations were conducted using a unified finite volume framework that integrates a compressible NSF airflow solver, an Eulerian droplet impingement solver, a PDE-based ice solver, and a multilayer heat conduction solver. The low-fidelity solver, however, was simplified by omitting heat dissipation in the solid domain.

Training an accurate surrogate model requires substantial computational resources to carry out a sufficient number of high-fidelity simulations and adequately cover the design space. In the specific case of this study, developing an accurate surrogate model based solely on high-fidelity simulations required at least 400 simulations, each taking approximately 24 hours. The multi-fidelity surrogate model reduced the required number of high-fidelity simulations by 75% (from 400 to 100) by leveraging low-fidelity simulations, which have negligible computational cost (approximately three minutes per simulation).

Additionally, proper orthogonal decomposition (POD) was employed to reduce the dimensionality of both high- and low-fidelity outputs by 60% (from 201 to 80 modes), while retaining 99.9% of the original information. Multi-fidelity Gaussian process regression (MFGPR), combined with POD, was then used to model the temperature distribution under stratiform cloud icing and continuous maximum icing envelope conditions, achieving prediction accuracies exceeding 95%.

Model accuracy was further validated through leave-one-out cross-validation (LOOCV), and adaptability was enhanced using a dynamically updated surrogate via a self-organizing map (SOM) combined with k-means clustering to incorporate new samples across the design space. This MFGPR–POD and GPR–POD surrogate reduced computational time by 99.998% (from 1,444 minutes to 0.03 minutes).

The optimization framework was constructed based on the multi-fidelity surrogate model to minimize the total electric power consumed by the heater pads. Regime-dependent constraints were imposed to ensure safe and effective operation, with maximum ice growth and target wall temperature applied in the running-wet mode, and both end-film height and maximum ice growth enforced in the evaporative mode.

The mesh adaptive direct search (MADS) algorithm, implemented through the NOMAD software, guided the iterative search by generating candidate heater power distributions and updating them based on surrogate model evaluations. The optimization results indicated reductions in total electric power consumption of 38.5% and 28% compared with the baseline configuration in the running-wet regime when applying the target wall temperature and maximum ice growth constraints, respectively. In the evaporative regime, a 40% improvement was achieved under the combined end film height– maximum ice growth constraint, confirming the effectiveness of the framework in enhancing performance across different operational conditions.

This investigation lays the groundwork, but it has several limitations and warrants further research. First, because this study was applied to a limited set of icing conditions, the current method needs to be expanded to cover the full range of icing conditions. This would be especially beneficial because the surrogate model does not need a lot of expensive high-fidelity simulations to be trained. Second, while the current process is optimized for ETIPSs in anti-icing mode, its flexibility needs to be verified by applying it to other operational modes, like de-icing, or to different ice protection methods, such as mechanical or other thermal systems.

## Declaration of competing interest

The authors declare that they have no known competing financial interests or personal relationships that could have appeared to influence the work reported in this paper.

## Data availability

No data was used for the research described in the article.

## Acknowledgments

This work was supported by the National Research Foundation of Korea (NRF) grant funded by the Korean government (MSIT) (RS-2024-00397400).

## References

[1] Y. Liu, Q. Yang, Q. Wang, X. Guo, X. Bu, X. Yi, Investigations on optimization and verification of nacelle hot air anti-icing system in a large icing wind tunnel, Aerospace Science and Technology (2025) 110312.

[2] J.H. Page, I. Ozcer, A. Zanon, M. De Gennaro, R.C. Llamas-Sandin, Aerodynamics and ice tolerance of the large passenger aircraft advanced rear end forward swept horizontal tailplane with leading edge extension, Aerospace Science and Technology 161 (2025) 110018.
[3] W.T. Lee, D.J. Hong, Y.W. Nam, R.S. Myong, Numerical and experimental investigation of multifunctional high-efficiency anti-icing nickel-plated carbon fiber heating elements for wing-shaped composite airfoils, Aerospace Science and Technology (2025) 110249.
[4] L. Tian, J. Tu, L. Feng, H. Liu, W. Tian, N. Han, Experimental Study on the Critical Icicles Evolution and icing-induced performance degradation over the propeller of UAVs, Aerospace Science and Technology (2025) 110777.
[5] E. Esmaeilifar, B. Sengupta, L. Prince Raj, R.S. Myong, In-flight anti-icing simulation of electrothermal ice protection systems with inhomogeneous thermal boundary condition, Aerospace Science and Technology 150 (2024) 109210.
[6] L. Prince Raj, High-Fidelity Computational Modeling of In-Flight Ice Accretion on Aircraft and Rotorcraft Including Supercooled Large Droplet, Ph. D. Thesis, Gyeongsang National University, 2017.
[7] R. Roy, L. Prince Raj, J.-H. Jo, M.-Y. Cho, J.-H. Kweon, R.S. Myong, Multiphysics anti-icing simulation of a CFRP composite wing structure embedded with thin etched-foil electrothermal heating films in glaze ice conditions, Composite Structures 276 (2021) 114441.
[8] L. Prince Raj, J. Lee, R.S. Myong, Ice accretion and aerodynamic effects on a multi-element airfoil under SLD icing conditions, Aerospace Science and Technology 85 (2019) 320-333.
[9] B.A. Gutiérrez, A. Della Noce, M. Gallia, T. Bellosta, A. Guardone, Numerical simulation of a thermal Ice Protection System including state-of-the-art liquid film model, Journal of Computational and Applied Mathematics 391 (2021) 113454.
[10] P. Yang, H. Li, J. Chen, Y. Duan, Y. Zhang, Influence of air flow field computation on an ice accretion simulation of airfoils, Aerospace Science and Technology 151 (2024) 109315.
[11] B. Sengupta, L. Prince Raj, M. Cho, C. Son, T. Yoon, K. Yee, R.S. Myong, Computational simulation of ice accretion and shedding trajectory of a rotorcraft in forward flight with strong rotor wakes, Aerospace Science and Technology 119 (2021) 107140.
[12] B. Bornhoft, S.S. Jain, K. Goc, S.T. Bose, P. Moin, Large-eddy simulations of the NACA23012 airfoil with laser-scanned ice shapes, Aerospace Science and Technology 146 (2024) 108957.
[13] B. Sengupta, E. Esmaeilifar, M. Sadegh Araghizadeh, S. Kang, H. Lee, R.S. Myong, L. Prince Raj, Rotor-Fuselage-Intake Aerodynamics and Icing Using Vortex and Eulerian–

Lagrangian Computational Fluid Dynamics Methods, AIAA Journal 63 (2025) 909-930.
[14] E. Esmaeilifar, L. Prince Raj, R.S. Myong, Computational simulation of aircraft electrothermal de-icing using an unsteady formulation of phase change and runback water in a unified framework, Aerospace Science and Technology 130 (2022) 107936.
[15] L. Prince Raj, R.S. Myong, Computational analysis of an electro-thermal ice protection system in atmospheric icing conditions, Journal of Computational Fluids Engineering 21 (2016) 1-9.
[16] Y.M. Lee, J.H. Lee, L. Prince Raj, J.H. Jo, R.S. Myong, Large-eddy simulations of complex aerodynamic flows over multi-element iced airfoils, Aerospace Science and Technology 109 (2021) 106417.
[17] M. Pourbagian, W.G. Habashi, Surrogate-based optimization of electrothermal wing anti-icing systems, Journal of Aircraft 50 (2013) 1555-1563.
[18] C. Audet, J.E. Dennis Jr, Mesh adaptive direct search algorithms for constrained optimization, SIAM Journal on Optimization 17 (2006) 188-217.
[19] M. Pourbagian, Multidisciplinary optimization of in-flight electro-thermal ice protection systems, McGill University (Canada), 2014.
[20] M. Pourbagian, B. Talgorn, W.G. Habashi, M. Kokkolaras, S. Le Digabel, Constrained problem formulations for power optimization of aircraft electro-thermal anti-icing systems, Optimization and Engineering 16 (2015) 663-693.
[21] A. Targui, W.G. Habashi, On a reduced-order model-based optimization of rotor electro-thermal anti-icing systems, International Journal of Numerical Methods for Heat & Fluid Flow 32 (2022) 2885-2913.
[22] S.K. Jung, L. Prince Raj, A. Rahimi, H. Jeong, R.S. Myong, Performance evaluation of electrothermal anti-icing systems for a rotorcraft engine air intake using a meta model, Aerospace Science and Technology 106 (2020) 106174.
[23] B. Arizmendi Gutiérrez, A. Della Noce, M. Gallia, A. Guardone, Optimization of a Thermal Ice Protection System by means of a genetic algorithm, in: International Conference on Bioinspired Methods and Their Applications, Springer, 2020.
[24] M. Gallia, G. Gori, A. Guardone, Numerical Optimization of Electrothermal Ice Protection Systems, in: Handbook of Numerical Simulation of In-Flight Icing, Springer, 2023, pp. 1123-1157.
[25] A.I. Forrester, A. Sóbester, A.J. Keane, Multi-fidelity optimization via surrogate modelling, Proceedings of the Royal Society A: Mathematical, Physical and Engineering

Sciences 463 (2007) 3251-3269.
[26] J. Fu, F. Qu, Q. Liu, D. Sun, J. Bai, Multi-objective aerodynamic optimization of two-dimensional hypersonic forebody-inlet based on the heuristic algorithm, Aerospace Science and Technology 123 (2022) 107470.
[27] C. Poggi, M. Rossetti, G. Bernardini, U. Iemma, C. Andolfi, C. Milano, M. Gennaretti, Surrogate models for predicting noise emission and aerodynamic performance of propellers, Aerospace Science and Technology 125 (2022) 107016.
[28] X. Geng, P. Liu, T. Hu, Q. Qu, J. Dai, C. Lyu, Y. Ge, R.A. Akkermans, Multi-fidelity optimization of a quiet propeller based on deep deterministic policy gradient and transfer learning, Aerospace Science and Technology 137 (2023) 108288.
[29] Q. Lin, J. Hu, Q. Zhou, Parallel multi-objective Bayesian optimization approaches based on multi-fidelity surrogate modeling, Aerospace Science and Technology 143 (2023) 108725.
[30] F. Tejero, D. MacManus, J. Hueso-Rebassa, F. Sanchez-Moreno, I. Goulos, C. Sheaf, Aerodynamic optimisation of civil aero-engine nacelles by dimensionality reduction and multi-fidelity techniques, International Journal of Numerical Methods for Heat & Fluid Flow 33 (2023) 1336-1353.
[31] F. Cao, Z. Tang, C. Zhu, X. He, Data-driven hierarchical collaborative optimization method with multi-fidelity modeling for aerodynamic optimization, Aerospace Science and Technology 150 (2024) 109206.
[32] X. Wu, Z. Zuo, L. Ma, W. Zhang, Multi-fidelity neural network-based aerodynamic optimization framework for propeller design in electric aircraft, Aerospace Science and Technology 146 (2024) 108963.
[33] Y. Zhang, Z.-h. Han, W.-p. Song, An efficient robust aerodynamic design optimization method based on a multi-level hierarchical Kriging model and multi-fidelity expected improvement, Aerospace Science and Technology 152 (2024) 109401.
[34] L. Prince Raj, E. Esmaeilifar, B. Sengupta, H. Jeong, R.S. Myong, Coarray Fortran parallel implementation of a finite volume method-based aircraft ice accretion simulation code, International Journal of Aeronautical and Space Sciences 24 (2023) 1124-1135.
[35] R.K. Jeck, Icing Design Envelopes (14 CFR Parts 25 and 29, Appendix C), Converted to a Distance-Based, Federal Aviation Administration, US Department of Transportation: Washington, DC, USA (2002).
[36] S.K. Jung, R.S. Myong, A second-order positivity-preserving finite volume upwind scheme for air-mixed droplet flow in atmospheric icing, Comput. Fluids 86 (2013) 459-469.

[37] L. Prince Raj, K. Yee, R.S. Myong, Sensitivity of ice accretion and aerodynamic performance degradation to critical physical and modeling parameters affecting airfoil icing, Aerosp. Sci. Technol. 98 (2020) 105659.
[38] T. Verstraete, S. Scholl, Stability analysis of partitioned methods for predicting conjugate heat transfer, Int. J. Heat Mass Transfer 101 (2016) 852-869.
[39] M.D. McKay, Latin hypercube sampling as a tool in uncertainty analysis of computer models, in: Proceedings of the 24th Conference on Winter Simulation, 1992.
[40] V. Klema, A. Laub, The singular value decomposition: Its computation and some applications, IEEE Transactions on Automatic Control 25 (1980) 164-176.
[41] S.K. Jung, R.S. Myong, T.-H. Cho, Development of Eulerian droplets impingement model using HLLC Riemann solver and POD-based reduced order method, in: 41st AIAA Fluid Dynamics Conference and Exhibit, 2011.
[42] S.K. Jung, R.S. Myong, T.H. Cho, Efficient Prediction of Ice Shapes in CFD Simulation of In-flight Icing Using a POD-Based Reduced Order Model, 0148-7191, SAE Technical Paper, 2011.
[43] S.K. Jung, S. Shin, R.S. Myong, T.H. Cho, An efficient CFD-based method for aircraft icing simulation using a reduced order model, Journal of Mechanical Science and Technology 25 (2011) 703-711.
[44] L. Cicci, S. Fresca, M. Guo, A. Manzoni, P. Zunino, Uncertainty quantification for nonlinear solid mechanics using reduced order models with Gaussian process regression, Computers & Mathematics with Applications 149 (2023) 1-23.
[45] Y. Yang, W. Zhao, Y. Xue, H. Yang, C. Wu, Improved automatic kernel construction for Gaussian process regression in small sample learning for predicting lift body aerodynamic performance, Physics of Fluids 35 (2023).
[46] Y. Yang, Y. Xue, W. Zhao, S. Yao, C. Li, C. Wu, Fast flow field prediction of three-dimensional hypersonic vehicles using an improved Gaussian process regression algorithm, Physics of Fluids 36 (2024).
[47] H. Zhang, J. Li, M. Yan, Y. Miao, Optimization of supersonic combustor configuration based on Gaussian process regression and genetic algorithm, Aerospace Science and Technology (2025) 109980.
[48] Z. Ma, W. Pan, Data-driven nonintrusive reduced order modeling for dynamical systems with moving boundaries using Gaussian process regression, Computer Methods in Applied Mechanics and Engineering 373 (2021) 113495.

[49] C.E. Rasmussen, Gaussian processes in machine learning, in: Summer School on Machine Learning, Springer, 2003, pp. 63-71.
[50] R. Dupuis, J.-C. Jouhaud, P. Sagaut, Aerodynamic data predictions for transonic flows via a machine-learning-based surrogate model, in: 2018 AIAA/ASCE/AHS/ASC Structures, Structural Dynamics, and Materials Conference, 2018.
[51] Z. Zhan, W.G. Habashi, M. Fossati, Local reduced-order modeling and iterative sampling for parametric analyses of aero-icing problems, AIAA Journal 53 (2015) 2174-2185.
[52] T. Kohonen, S.-O. Maps, Springer series in information sciences, Self-Organizing Maps 30 (1995).
[53] J. Hollmén, V. Tresp, O. Simula, A self-organizing map for clustering probabilistic models, in: 1999 Ninth International Conference on Artificial Neural Networks ICANN 99.(Conf. Publ. No. 470), IET, 1999.
[54] C. Audet, W. Hare, Model-based methods in derivative-free nonsmooth optimization, in: Bagirov, A., Gaudioso, M., Karmitsa, N., Mäkelä, M., Taheri, S. (eds) Numerical Nonsmooth Optimization, Springer, 2020.
[55] L.D.S. Audet C, Rochon Montplaisir V, Tribes C (n.d.), The NOMAD Software, [Online]. Available at: https://www.gerad.ca/en/software/nomad.
[56] K. Al-Khalil, C. Horvath, D. Miller, W. Wright, K. Al-Khalil, C. Horvath, D. Miller, W. Wright, Validation of NASA thermal ice protection computer codes. III-The validation of ANTICE, in: 35th Aerospace Sciences Meeting and Exhibit, 1997.
[57] X. Liu, W. Zhao, D. Wan, Multi-fidelity Co-Kriging surrogate model for ship hull form optimization, Ocean Engineering 243 (2022) 110239.